Chemistry–A European Journal

Supporting Information

Three Perovskite Phases with Different Cation Orders in $Sm_2MnMn(Mn_{4-x}Sb_x)O_{12}$

Xuan Liang, Kazunari Yamaura, and Alexei A. Belik*

Supporting Information

Three Perovskite Phases with Different Cation Orders in $Sm_2MnMn(Mn_{4-x}Sb_x)O_{12}$

Xuan Liang [a,b], Kazunari Yamaura [a,b], Alexei A. Belik [a,*]

[a] *Research Center for Materials Nanoarchitectonics (MANA), National Institute for Materials Science (NIMS), Namiki 1-1, Tsukuba, Ibaraki 305-0044, Japan*

[b] *Graduate School of Chemical Sciences and Engineering, Hokkaido University, North 10 West 8, Kita-ku, Sapporo, Hokkaido 060-0810, Japan*

* Corresponding author.

E-mail address: Alexei.Belik@nims.go.jp (A.A. Belik)

Experimental Part

Sample preparation. $Sm_2MnMn(Mn_{4-x}Sb_x)O_{12}$ samples with x = 0.4, 0.5, 0.6, 0.7, 0.8, 0.9, 1.0, 1.1, 1.4, 1.5, 1.6, 1.7, 1.8, 1.9, and 2.0 were prepared using stoichiometric mixtures of Sm_2O_3 (99.9 %), Sb_2O_3 (99.9 %), and Mn_2O_3, where Sm_2O_3 was dried in air at 1270 K for 1 h and the other two oxides were dried in air at 390 K for 4 h before use. Single-phase Mn_2O_3 was prepared from commercial MnO_2 (99.9 %) by heating in air at 920 K for 24 h. The mixtures were placed in Pt capsules and treated at 6 GPa in a belt-type high-pressure apparatus at about 1770 K for 2 hours (heating time to the desired temperature was 20 min). After the heat treatments, the samples were cooled to room temperature by turning off the heating current, and the pressure was slowly released.

X-ray powder diffraction. Room-temperature laboratory X-ray powder diffraction (XRPD) data were collected on a RIGAKU MiniFlex600 diffractometer using CuKα radiation (in a 2θ range of 8–100° with a step of 0.02°, and a scan speed of 3°/min). Room-temperature synchrotron XRPD data were collected on the BL02B2 beamline of SPring-8[29] between 1.95° and 78.09° with a constant interval of 0.006° in 2θ with the wavelength of λ = 0.42019 Å. The samples were placed into Lindemann glass capillary tubes (inner diameter: 0.2 mm), which were rotated during measurements. The Rietveld analysis of all XRPD data was performed using the *RIETAN-2000* program.[30] The synchrotron XRPD data up to 70.00° were used in the Rietveld analysis as no experimental reflections were observed between 70.00° and 78.09° (they were too weak).

Magnetic properties. Magnetic susceptibilities (χ = *M/H*) were measured on a SQUID magnetometer (Quantum Design, MPMS3) between 2 and 400 K in different applied magnetic fields under both zero-field-cooled (ZFC) and field-cooled on cooling (FCC) conditions. Before ZFC measurements, a reset-magnet procedure was applied to reduce a trapped magnetic field inside a magnetometer. FCC curves were recorded after ZFC measurements. The inverse magnetic susceptibilities (χ^{-1}) were fit by the Curie−Weiss equation.

$$\chi(T) = \mu_{\text{eff}}{}^2 N(3k_B(T-\theta))^{-1}$$

where μ_{eff} is the effective magnetic moment, N is Avogadro's number, k_B is Boltzmann's constant, and θ is the Curie−Weiss temperature. For fitting, we used the FCC

curves measured at 10 kOe and temperature intervals between 200 K and 395 K. Isothermal magnetization measurements (M versus H) were performed between −70 and 70 kOe at different temperatures.

Specific heat was measured on a commercial calorimeter (Quantum Design PPMS) on cooling at magnetic fields of 0 Oe and 90 kOe.

Additional Discussion

The c lattice parameter and T_C of the $Sm_2MnMn(Mn_{3.6}Sb_{0.4})O_{12}$ sample (x = 0.4) continue to change monotonically and do not match with the $Sm_2MnMn(Mn_{3.5}Sb_{0.5})O_{12}$ sample (x = 0.5) as would be expected for $Sm_2MnMn(Mn_{4-x}Sb_x)O_{12}$ solid solutions with the solubility limit near x = 0.5. These features could be explained by an additional composition variation. The $Sm_2MnMn(Mn_{3.6}Sb_{0.4})O_{12}$ sample had $SmMn_7O_{12}$ impurity (about 8 wt. %), which is Sm-poor in comparison with the target $Sm_2MnMn(Mn_{3.6}Sb_{0.4})O_{12}$ composition. Therefore, the main phase should be Sm-rich: $Sm_{2+y}Mn_{1-y}Mn(Mn_{4-x}Sb_x)O_{12}$. Indeed, the refinement of the crystal structure of the x = 0.4 sample (from synchrotron powder X-ray diffraction data at room temperature; results are not shown) gave the following composition: $Sm_{2.10}Mn_{0.90}Mn(Mn_{3.6}Sb_{0.4})O_{12}$ (with the fixed Sb content based on the target composition; the amount of the pyrochlore-type impurity in this sample (x = 0.4) was 1.6 wt. % (Figure S18)). In all other samples, the (freely) refined Sm content was smaller than that of the x = 0.4 sample and agreed well with the target compositions in many cases.

In the final structural models, the Sb content was fixed based on the target compositions because the refined occupation factors were very close to the expected ones (Tables S10–S13). In the tetragonal structures, the total Sm content was not fixed, but the occupations factors, g, of the Sm, Mn1, and Mn2 sites were just refined with the following constraints: g(Sm) + g(Mn) = 1 for the Sm and Mn2 sites and g(Sm) + g(Mn) = 0.5 for the split Mn1 site. The Sm content, refined in such a way, agreed well with the target compositions in many cases. The Sm content in the x = 1.8 sample was fixed to the nominal value in the final model because the refined occupation factor was very close to the expected one (Table S13).

Because of the presence of an unidentified impurity in the $Sm_2MnMn(Mn_2Sb_2)O_{12}$ sample (x = 2.0), only a ratio of the weight fractions of the phases (given on Figure 2 in the main text and on Figure S18) is relevant (not absolute values) (the amount of the pyrochlore-type impurity in this sample (x = 2.0) was 2.8 wt. %).

The x = 1.5 and 1.6 samples had a $GdFeO_3$-type *Pnma* impurity (about 6 wt. %). The $GdFeO_3$-type *Pnma* structure has one A site and one B site; therefore, all possible cations are disordered at the A site and at the B site. However, the chemical composition of the $GdFeO_3$-type *Pnma* impurity is not known, and it could significantly deviate from the target compositions. The phase was present in small amounts. Therefore, we cannot claim that the fourth perovskite phase (that is, in addition to the $P4_2/nmc$, $P4_2/n$, and $P2_1/n$ phases) was formed with the target composition.

We note that in addition to the nominal variation (as the variable x) of the chemical composition in $Sm_2MnMn(Mn_{4-x}Sb_x)O_{12}$, the presence of different amounts of different impurities can also slightly vary chemical compositions of the main phases. Therefore, the system can move between different phases in the vicinity of x = 2 also as a function of impurities (not only as a function of x).

Table S1. Lattice parameters and symmetry of $Sm_2MnMn(Mn_{4-x}Sb_x)O_{12}$ at $T = 295$ K from synchrotron X-ray powder diffraction data.

x	Symmetry	a (Å)	b (Å)	c (Å)	β (°)
0.4	$P4_2/nmc$	7.46151		7.96307	
0.5	$P4_2/nmc$	7.46910		7.96619	
0.6	$P4_2/nmc$	7.48014		7.96614	
0.7	$P4_2/nmc$	7.50953		7.94695	
0.8	$P4_2/nmc$	7.53536		7.92448	
0.9	$P4_2/nmc$	7.56748		7.89950	
1.0	$P4_2/nmc$	7.60131		7.88261	
1.1	$P4_2/nmc$	7.61131		7.87379	
	$P4_2/n$	7.70880		7.86524	
1.4	$P4_2/nmc$	7.62790		7.85699	
	$P4_2/n$	7.71198		7.86390	
1.5	$P4_2/n$	7.72306		7.86363	
1.6	$P4_2/n$	7.75512		7.85881	
1.7	$P4_2/n$	7.76709		7.85648	
	$P2_1/n$	5.41991	5.58726	7.84227	90.2908
1.8	$P2_1/n$	5.42746	5.58884	7.86242	90.2732
1.9	$P4_2/n$	7.80522		7.85344	
	$P2_1/n$	5.44235	5.60207	7.87506	90.2301
2.0	$P4_2/n$	7.81194		7.85250	
	$P2_1/n$	5.44356	5.60033	7.88457	90.2325

For tetragonal symmetries ($P4_2/nmc$ and $P4_2/n$), $a = b$ and $\alpha = \beta = \gamma = 90°$. For the monoclinic symmetry ($P2_1/n$), $\alpha = \gamma = 90°$.

Table S2. Structure parameters of $Sm_2MnMn(Mn_{4-x}Sb_x)O_{12}$ (x = 0.5, 0.6, and 0.7) at T = 295 K from synchrotron X-ray powder diffraction data.

x	0.5	0.6	0.7
Crystal system	Tetragonal		
Space group	$P4_2/nmc$ (No. 137, cell choice 2)		
a (Å)	7.46910(1)	7.48014(2)	7.50953(2)
c (Å)	7.96619(2)	7.96614(2)	7.94695(2)
V (Å^3)	444.4130(16)	445.725(2)	448.153(2)
g(Sm)	0.929(3)Sm+0.071Mn	0.913(3)Sm+0.087Mn	0.932(4)Sm+0.068Mn
z(Sm)	0.22105(5)	0.22132(6)	0.22070(7)
B(Sm) (Å^2)	1.061(8)	1.099(10)	1.181(12)
g(Mn1-SQ)	0.452(3)Mn+0.048Sm	0.446(3)Mn+0.054Sm	0.454(3)Mn+0.046Sm
z(Mn1)	0.7783(5)	0.7821(4)	0.7782(7)
B(Mn1) (Å^2)	1.78(8)	1.64(9)	2.21(12)
g(Mn2-T)	0.917(4)Mn+0.083Sm	0.935(4)Mn+0.065Sm	0.913(5)Mn+0.087Sm
B(Mn2) (Å^2)	0.62(5)	0.58(5)	0.71(6)
g(Mn/Sb-Oc)	0.875Mn+0.125Sb	0.85Mn+0.15Sb	0.825Mn+0.175Sb
B(Mn/Sb) (Å^2)	0.706(12)	0.759(15)	0.846(17)
y(O1)	0.0569(5)	0.0572(5)	0.0550(6)
z(O1)	–0.0409(5)	–0.0418(5)	–0.0388(6)
B(O1) (Å^2)	0.98(7)	0.96(8)	0.95(9)
y(O2)	0.5348(5)	0.5343(6)	0.5344(6)
z(O2)	0.5834(5)	0.5825(5)	0.5824(6)
B(O2) (Å^2)	1.34(9)	1.40(10)	0.99(10)
x(O3)	0.4330(4)	0.4335(4)	0.4338(5)
B(O3) (Å^2)	1.75(9)	2.64(12)	1.69(12)
R_{wp} (%)	7.42	7.97	9.24
R_p (%)	5.39	5.71	6.55
R_I (%)	4.67	4.48	5.80
R_F (%)	5.80	4.23	6.28
Impurities	pyrochlore-type phase (a = 10.2615 Å): 0.8 % $SmMn_7O_{12}$: 1.2 %	pyrochlore-type phase (a = 10.2672 Å): 1.2 %	pyrochlore-type phase (a = 10.2694 Å): 0.6 %

Crystal data: space group $P4_2/nmc$ (No. 137, cell choice 2), Z = 2.
Sm – 4*d* site (0.25, 0.25, *z*); Mn1-SQ – 4*c* site (0.75, 0.25, *z*) near 2*a* site (0.75, 0.25, 0.75); Mn2-T – 2*b* site (0.75, 0.25, 0.25); Mn/Sb-Oc – 8*e* site (0, 0, 0); O1 and O2 – 8*g* site (0.25, *y*, *z*), and O3 – 8*f* site (*x*, –*x*, 0.25).
g(O1) = g(O2) = g(O3) = 1, g is the occupation factor.
SQ: square-planar (site), T: tetrahedral (site), Oc: octahedral (site).

Table S3. Bond lengths, bond angles, bond-valence sum (BVS), and distortion parameters of $(Mn/Sb)O_6$ (Δ) in $Sm_2MnMn(Mn_{4-x}Sb_x)O_{12}$ (x = 0.5, 0.6, and 0.7) at T = 295 K from synchrotron X-ray powder diffraction data.

x	0.5	0.6	0.7
Sm-O1 (Å) ×2	2.383(4)	2.375(4)	2.408(5)
Sm-O1 (Å) ×2	2.537(4)	2.544(4)	2.529(5)
Sm-O2 (Å) ×2	2.391(4)	2.397(4)	2.402(4)
Sm-O3 (Å) ×4	2.744(1)	2.746(1)	2.756(1)
BVS(Sm^{3+})	+3.06	+3.05	+2.96
Mn1-O3 (Å) ×4	1.946(4)	1.958(5)	1.965(5)
Mn1-O2 (Å) ×2	2.915(5)	2.887(5)	2.910(6)
Mn1-O1 (Å) ×2	3.103(5)	3.092(5)	3.088(6)
Mn1-Mn1	0.451(8)	0.511(7)	0.448(11)
BVS($Mn1^{3+}$)	+2.56	+2.50	+2.44
BVS($Mn1^{2+}$)	+2.78	+2.71	+2.65
Mn2-O2 (Å) ×4	2.086(4)	2.094(4)	2.097(5)
Mn2-O1 (Å) ×4	2.834(4)	2.834(4)	2.840(5)
BVS($Mn2^{2+}$)	+2.03	+2.00	+1.98
Mn/Sb-O1 (Å) ×2	1.943(1)	1.947(1)	1.947(1)
Mn/Sb-O2 (Å) ×2	1.999(1)	1.999(2)	2.005(2)
Mn/Sb-O3 (Å) ×2	2.114(1)	2.112(2)	2.107(2)
Δ(Mn/Sb)	1.2×10^{-3}	1.2×10^{-3}	1.1×10^{-3}
BVS(Mn^{3+})	+3.04	+3.03	+3.02
BVS(Sb^{5+})	+4.97	+4.95	+4.94
Mn/Sb-O1-Mn/Sb×2	148.0(3)	147.7(3)	149.3(3)
Mn/Sb-O2-Mn/Sb×2	138.2(3)	138.7(3)	138.9(3)
Mn/Sb-O3-Mn/Sb×2	140.85(10)	141.07(12)	141.03(13)

$BVS = \sum_{i=1}^{N} v_i$, $v_i = \exp[(R_0 - l_i)/B]$, N is the coordination number, B = 0.37, $R_0(Sm^{3+})$ = 2.088, $R_0(Mn^{2+})$ = 1.79, $R_0(Mn^{3+})$ = 1.76, $R_0(Sb^{5+})$ = 1.942.[31]

Table S4. Structure parameters of $Sm_2MnMn(Mn_{4-x}Sb_x)O_{12}$ (x = 0.8, 0.9, and 1.0) at T = 295 K from synchrotron X-ray powder diffraction data.

x	0.8	0.9	1.0
Crystal system	Tetragonal		
Space group	$P4_2/nmc$ (No. 137, cell choice 2)		
a (Å)	7.53536(2)	7.56748(2)	7.60131(2)
c (Å)	7.92448(2)	7.89950(2)	7.88261(2)
V (Å^3)	449.9652(17)	452.379(2)	445.456(2)
g(Sm)	0.922(3)Sm+0.078Mn	0.904(3)Sm+0.096Mn	0.912(3)Sm+0.088Mn
z(Sm)	0.22098(6)	0.22110(7)	0.22133(6)
B(Sm) (Å^2)	1.173(10)	1.292(10)	1.291(11)
g(Mn1-SQ)	0.446(3)Mn+0.054Sm	0.440(3)Mn+0.060Sm	0.433(3)Mn+0.067Sm
z(Mn1)	0.7805(5)	0.7810(5)	0.7891(4)
B(Mn1) (Å^2)	1.78(9)	2.13(10)	1.96(9)
g(Mn2-T)	0.905(5)Mn+0.095Sm	0.912(4)Mn+0.088Sm	0.939(4)Mn+0.061Sm
B(Mn2) (Å^2)	0.85(5)	0.84(6)	0.67(5)
g(Mn/Sb-Oc)	0.8Mn+0.2Sb	0.775Mn+0.225Sb	0.75Mn+0.25Sb
B(Mn/Sb) (Å^2)	0.776(13)	0.896(15)	0.825(14)
y(O1)	0.0582(5)	0.0562(5)	0.0661(5)
z(O1)	–0.0373(5)	–0.0398(5)	–0.0373(5)
B(O1) (Å^2)	0.72(7)	0.86(8)	1.35(9)
y(O2)	0.5353(5)	0.5373(5)	0.5381(5)
z(O2)	0.5799(5)	0.5817(5)	0.5804(5)
B(O2) (Å^2)	0.94(9)	1.05(10)	1.42(10)
x(O3)	0.4349(4)	0.4344(4)	0.4401(4)
B(O3) (Å^2)	1.81(10)	2.66(12)	1.95(10)
R_{wp} (%)	7.32	7.14	7.36
R_p (%)	5.24	5.10	5.20
R_I (%)	6.02	5.33	4.46
R_F (%)	5.62	6.66	6.35
Impurities	pyrochlore-type phase (a = 10.2712 Å): 2.5 %	pyrochlore-type phase (a = 10.2743 Å): 2.1 %	pyrochlore-type phase (a = 10.2765 Å): 1.5 %

Crystal data: space group $P4_2/nmc$ (No. 137, cell choice 2), Z = 2.
Sm – 4*d* site (0.25, 0.25, *z*); Mn1-SQ – 4*c* site (0.75, 0.25, *z*) near 2*a* site (0.75, 0.25, 0.75); Mn2-T – 2*b* site (0.75, 0.25, 0.25); Mn/Sb-Oc – 8*e* site (0, 0, 0); O1 and O2 – 8*g* site (0.25, *y*, *z*), and O3 – 8*f* site (*x*, –*x*, 0.25).
g(O1) = g(O2) = g(O3) = 1, g is the occupation factor.
SQ: square-planar (site), T: tetrahedral (site), Oc: octahedral (site).

Table S5. Bond lengths, bond angles, bond-valence sum (BVS), and distortion parameters of $(Mn/Sb)O_6$ (Δ) in $Sm_2MnMn(Mn_{4-x}Sb_x)O_{12}$ (x = 0.8, 0.9, and 1.0) at T = 295 K from synchrotron X-ray powder diffraction data.

x	0.8	0.9	1.0
Sm-O1 (Å) ×2	2.400(4)	2.392(4)	2.361(4)
Sm-O1 (Å) ×2	2.506(4)	2.530(4)	2.472(4)
Sm-O2 (Å) ×2	2.423(4)	2.437(4)	2.456(4)
Sm-O3 (Å) ×4	2.763(10)	2.776(1)	2.773(1)
BVS(Sm^{3+})	+2.96	+2.89	+3.03
Mn1-O3 (Å) ×4	1.985(4)	1.988(4)	2.067(4)
Mn1-O2 (Å) ×2	2.872(5)	2.870(5)	2.805(5)
Mn1-O1 (Å) ×2	3.088(5)	3.090(5)	3.098(5)
Mn1-Mn1	0.483(8)	0.489(8)	0.617(6)
BVS($Mn1^{3+}$)	+2.33	+2.31	+1.92
BVS($Mn1^{2+}$)	+2.53	+2.51	+2.08
Mn2-O2 (Å) ×4	2.106(4)	2.088(4)	2.093(4)
Mn2-O1 (Å) ×4	2.870(4)	2.851(4)	2.930(4)
BVS($Mn2^{2+}$)	+1.92	+2.02	+1.95
Mn/Sb-O1 (Å) ×2	1.957(1)	1.964(1)	1.988(1)
Mn/Sb-O2 (Å) ×2	2.005(1)	2.019(1)	2.024(2)
Mn/Sb-O3 (Å) ×2	2.099(1)	2.096(2)	2.073(1)
Δ(Mn/Sb)	8.6×10^{-4}	7.1×10^{-4}	3.0×10^{-4}
BVS(Mn^{3+})	+3.01	+2.95	+2.92
BVS(Sb^{5+})	+4.92	+4.83	+4.77
Mn/Sb-O1-Mn/Sb×2	148.7(3)	148.8(3)	145.9(3)
Mn/Sb-O2-Mn/Sb×2	139.9(3)	139.1(3)	139.7(3)
Mn/Sb-O3-Mn/Sb×2	141.39(11)	140.83(12)	143.82(11)

$BVS = \sum_{i=1}^{N} v_i$, $v_i = \exp[(R_0 - l_i)/B]$, N is the coordination number, B = 0.37, $R_0(Sm^{3+})$ = 2.088, $R_0(Mn^{2+})$ = 1.79, $R_0(Mn^{3+})$ = 1.76, $R_0(Sb^{5+})$ = 1.942.[31]

Table S6. Structure parameters of $Sm_2MnMn(Mn_{4-x}Sb_x)O_{12}$ (x = 1.5 and 1.6) at T = 295 K from synchrotron X-ray powder diffraction data.

x	1.5	1.6
Crystal system	Tetragonal	
Space group	$P4_2/n$ (No. 86, cell choice 2)	
a (Å)	7.72306(5)	7.75512(5)
c (Å)	7.86363(4)	7.85881(4)
V (Å^3)	469.032(5)	472.643(5)
g(Sm)	0.911(4)Sm+0.089Mn	0.908(4)Sm+0.092Mn
z(Sm)	0.77822(8)	0.77827(8)
B(Sm) (Å^2)	1.053(17)	0.923(16)
g(Mn1-SQ)	0.421(4)Mn+0.079Sm	0.426(3)Mn+0.074Sm
z(Mn1)	0.7903(5)	0.7879(5)
B(Mn1) (Å^2)	2.05(12)	2.07(12)
g(Mn2-T)	0.973(5)Mn+0.027Sm	1Mn
B(Mn2) (Å^2)	0.31(7)	0.11(5)
g(Mn3-Oc)	1Mn	1Mn
B(Mn3) (Å^2)	0.82(4)	0.86(4)
g(Sb/Mn-Oc)	0.75Sb+0.25Mn	0.8Sb+0.2Mn
B(Sb/Mn) (Å^2)	0.58(2)	0.438(17)
x(O1)	–0.0438(13)	–0.0437(13)
y(O1)	0.5731(13)	0.5755(12)
z(O1)	0.2378(9)	0.2354(8)
B(O1) (Å^2)	1.22(17)	1.14(17)
x(O2)	–0.2388(21)	–0.2379(19)
y(O2)	–0.0370(8)	–0.0377(8)
z(O2)	0.5845(7)	0.5834(7)
B(O2) (Å^2)	1.74(16)	1.52(16)
x(O3)	–0.2558(19)	–0.2589(17)
y(O3)	0.0731(7)	0.0713(7)
z(O3)	–0.0357(7)	–0.0349(7)
B(O3) (Å^2)	1.80(15)	1.22(14)
R_{wp} (%)	7.38	7.56
R_p (%)	5.22	5.64
R_I (%)	3.26	2.85
R_F (%)	3.06	2.06
Impurities	pyrochlore-type phase (a = 10.2891 Å): 3.9 %	pyrochlore-type phase (a = 10.2929 Å): 2.3 %
	Pnma-per. (a = 5.6391 Å, b = 7.6247 Å, c = 5.3654 Å): 5.7 %	*Pnma*-per. (a = 5.6843 Å, b = 7.5832 Å, c = 5.3658 Å): 6.6 %

Crystal data: space group $P4_2/n$ (No. 86, cell choice 2), $Z = 2$.
Sm – 4*e* site (0.25, 0.75, *z*); Mn1-SQ – 4*f* site (0.25, 0.25, *z*) near 2*b* site (0.25, 0.25, 0.75); Mn2-T – 2*a* site (0.75, 0.75, 0.75); Mn3-Oc – 4*c* site (0, 0.5, 0.5); Sb/Mn-Oc – 4*d* site (0, 0, 0.5); O1, O2 and O3 – 8*g* site (*x*, *y*, *z*).
g(O1) = *g*(O2) = *g*(O3) = 1, *g* is the occupation factor.
SQ: square-planar (site), T: tetrahedral (site), Oc: octahedral (site).
Pnma-per.: a $GdFeO_3$-type perovskite phase with *Pnma* symmetry.

Table S7. Bond lengths, bond angles, bond-valence sum (BVS), and distortion parameters of $Mn3O_6$ and $(Sb/Mn)O_6$ (Δ) in $Sm_2MnMn(Mn_{4-x}Sb_x)O_{12}$ (x = 1.5 and 1.6) at T = 295 K from synchrotron X-ray powder diffraction data.

x	1.5	1.6
Sm-O1 (Å) ×2	2.668(13)	2.671(12)
Sm-O1 (Å) ×2	2.963(13)	2.991(12)
Sm-O2 (Å) ×2	2.467(6)	2.484(6)
Sm-O3 (Å) ×2	2.347(5)	2.363(6)
Sm-O3 (Å) ×2	2.443(6)	2.448(6)
BVS(Nd^{3+})	+3.08	+2.98
Mn1-O3 (Å) ×2	3.155(6)	3.159(7)
Mn1-O2 (Å) ×2	2.840(6)	2.848(7)
Mn1-O1 (Å) ×2	2.110(6)	2.104(6)
Mn1-O1 (Å) ×2	2.139(6)	2.136(6)
Mn1-Mn1	0.633(8)	0.596(8)
BVS($Mn1^{2+}$)	+1.79	+1.81
Mn2-O3 (Å) ×4	3.011(6)	3.012(6)
Mn2-O2 (Å) ×4	2.099(6)	2.106(6)
BVS($Mn2^{2+}$)	+1.88	+1.85
Mn3-O1 (Å) ×2	2.164(7)	2.186(7)
Mn3-O2 (Å) ×2	2.143(15)	2.156(14)
Mn3-O3 (Å) ×2	2.073(14)	2.100(13)
Δ(Mn3)	3.3×10^{-4}	2.7×10^{-4}
BVS($Mn3^{2+}$)	+2.43	+2.29
Sb/Mn-O1 (Å) ×2	1.982(7)	1.970(7)
Sb/Mn-O2 (Å) ×2	1.981(15)	1.979(7)
Sb/Mn-O3 (Å) ×2	1.989(14)	1.969(12)
Δ(Sb/Mn)	2.9×10^{-6}	5.5×10^{-6}
BVS(Sb^{5+})	+5.35	+5.52
BVS(Mn^{3+})	+3.27	+3.36
Mn3-O1-Sb/Mn ×2	142.9(6)	141.9(5)
Mn3-O2-Sb/Mn ×2	138.9(3)	139.3(4)
Mn3-O3-Sb/Mn ×2	143.8(3)	144.6(3)

$\text{BVS} = \sum_{i=1}^{N} v_i$, $v_i = \exp[(R_0 - l_i)/B]$, N is the coordination number, B = 0.37, $R_0(Sm^{3+})$ = 2.088, $R_0(Mn^{2+})$ = 1.79, $R_0(Mn^{3+})$ = 1.76, $R_0(Sb^{5+})$ = 1.942.[31]

Table S8. Structure parameters of $Sm_2MnMn(Mn_{4-x}Sb_x)O_{12}$ (x = 1.8) at T = 295 K from synchrotron X-ray powder diffraction data.

x	1.8
Crystal system	Monoclinic
Space group	$P2_1/n$ (No. 14, cell choice 2)
a (Å)	5.42746(2)
b (Å)	5.58884(2)
c (Å)	7.86242(2)
β (°)	90.2732(2)
V (Å^3)	238.4900(14)
x(Sm/Mn)	0.01118(12)
y(Sm/Mn)	0.05300(6)
z(Sm/Mn)	0.74769(8)
g(Sm/Mn)	0.5Sm+0.5Mn
B(Sm/Mn) (Å^2)	0.882(9)
g(Mn-Oc)	1Mn
B(Mn) (Å^2)	0.75(3)
g(Sb/Mn-Oc)	0.9Sb+0.1Mn
B(Sb/Mn) (Å^2)	0.618(13)
x(O1)	0.3011(7)
y(O1)	0.3111(7)
z(O1)	0.9458(5)
B(O1) (Å^2)	1.36(9)
x(O2)	0.3190(7)
y(O2)	0.2951(7)
z(O2)	0.5615(5)
B(O2) (Å^2)	1.42(10)
x(O3)	0.8818(6)
y(O3)	0.4340(7)
z(O3)	0.7646(5)
B(O3) (Å^2)	1.50(8)
R_{wp} (%)	5.51
R_p (%)	4.09
R_I (%)	3.37
R_F (%)	2.69
Impurities	pyrochlore-type phase (a = 10.2970 Å): 5.0 %

Crystal data: space group $P2_1/n$ (No. 14, cell choice 2), Z = 2.
Sm/Mn – 4*e* site (x, y, z); Mn-Oc – 2*d* site (0.5, 0, 0); Sb/Mn-Oc – 2*c* site (0, 0.5, 0); O1, O2 and O3 – 4*e* site (x, y, z).
g(O1) = g(O2) = g(O3) = 1, g is the occupation factor. Oc: octahedral (site).

Table S9. Bond lengths, bond angles, bond-valence sum (BVS), and distortion parameters of MnO_6 and $(Sb/Mn)O_6$ (Δ) in $Sm_2MnMn(Mn_{4-x}Sb_x)O_{12}$ (x = 1.8) at T = 295 K from synchrotron X-ray powder diffraction data.

x	1.8
Sm/Mn-O1 (Å)	2.275(4)
Sm/Mn-O1 (Å)	2.638(4)
Sm/Mn-O1 (Å)	2.738(4)
Sm/Mn-O2 (Å)	2.273(4)
Sm/Mn-O2 (Å)	2.603(4)
Sm/Mn-O2 (Å)	2.817(4)
Sm/Mn-O3 (Å)	2.234(3)
Sm/Mn-O3 (Å)	2.250(4)
BVS(M^{n+})	+2.22
Mn-O1 (Å) ×2	2.099(4)
Mn-O2 (Å) ×2	2.139(4)
Mn-O3 (Å) ×2	2.217(4)
Δ(Mn)	5.2×10^{-4}
BVS($Mn1^{2+}$)	+2.28
Sb/Mn-O1 (Å) ×2	1.986(4)
Sb/Mn-O2 (Å) ×2	1.972(4)
Sb/Mn-O3 (Å) ×2	1.984(4)
Δ(Sb/Mn)	9.6×10^{-6}
BVS(Sb^{5+})	+5.40
BVS(Mn^{3+})	+3.30
Mn-O1-Sb/Mn ×2	145.1(3)
Mn-O2-Sb/Mn ×2	142.8(3)
Mn-O3-Sb/Mn ×2	138.63(18)

$\text{BVS} = \sum_{i=1}^{N} v_i$, $v_i = \exp[(R_0 - l_i)/B]$, N is the coordination number, B = 0.37, $R_0(Sm^{3+})$ = 2.088, $R_0(Mn^{2+})$ = 1.79, $R_0(M^{n+})$ = 1.939 (an average of Sm^{3+} + Mn^{2+}), $R_0(Mn^{3+})$ = 1.76, $R_0(Sb^{5+})$ = 1.942.[31]

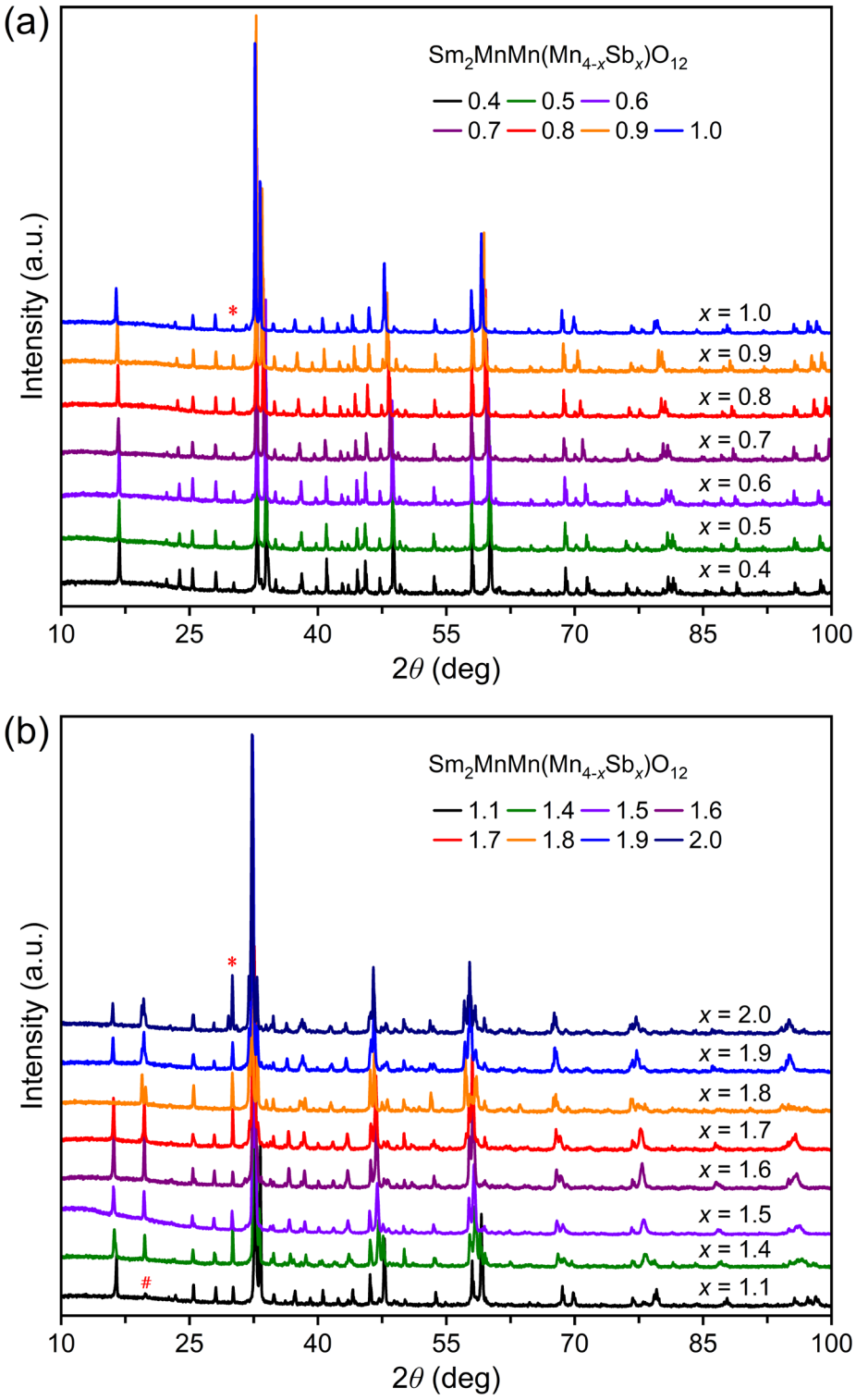

Figure S1a and S1b. X-ray powder diffraction patterns of $Sm_2MnMn(Mn_{4-x}Sb_x)O_{12}$ with a) $0.4 \le x \le 1.0$ and b) $1.1 \le x \le 2.0$ at $T = 295$ K (CuKα radiation). The red asterisk shows the 100% peak of a pyrochlore-type phase. The red octothorpe shows a characteristic peak of the $P4_2/n$ phase (with the Miller index of (111)).

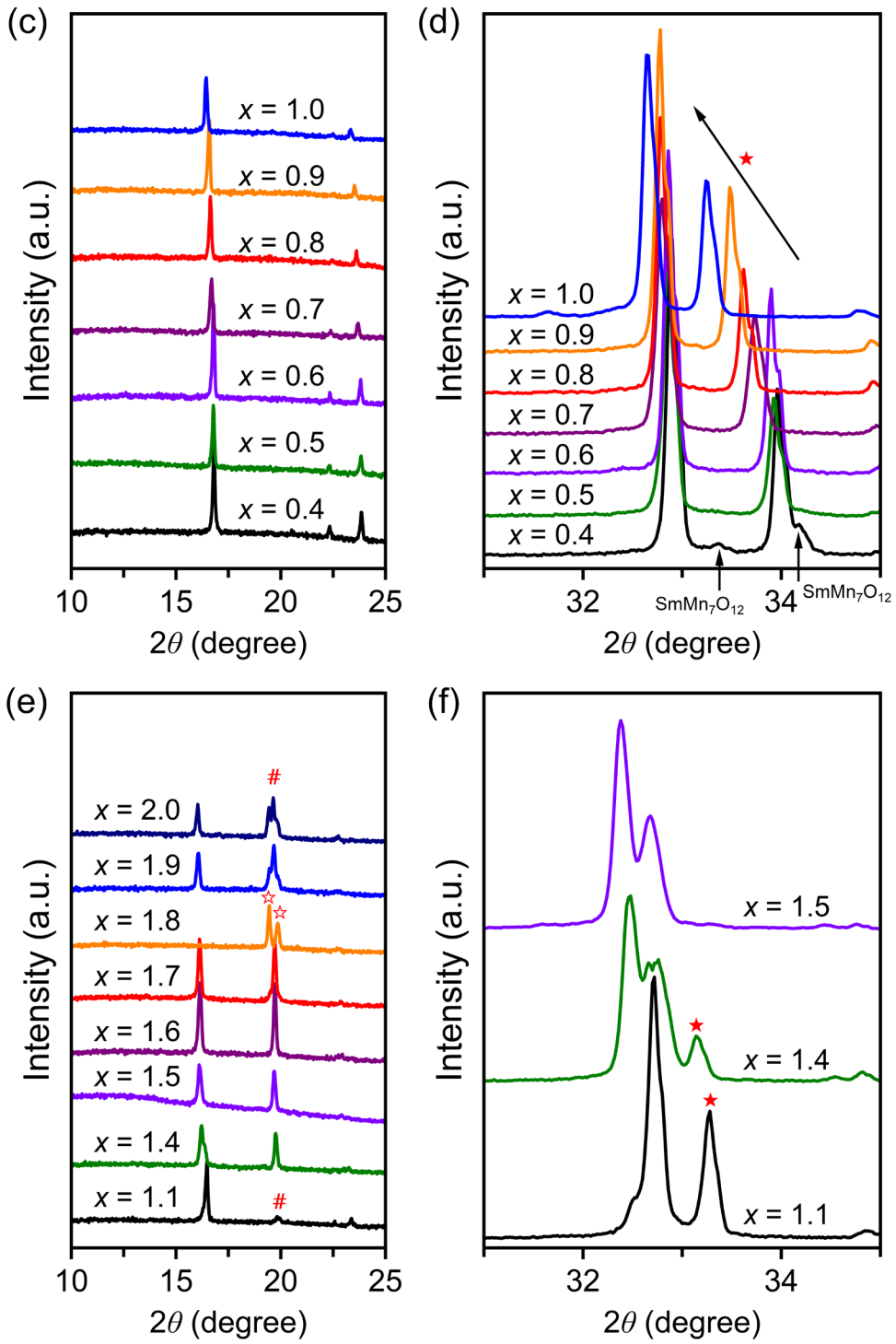

Figure S1c–S1f. Fragments of X-ray powder diffraction patterns of $Sm_2MnMn(Mn_{4-x}Sb_x)O_{12}$ at different x values at T = 295 K (CuKα radiation). The red octothorpe on panel (e) shows a characteristic peak of the $P4_2/n$ phase (with the Miller index of (111)). The full, red stars show a characteristic peak of the $P4_2/nmc$ phase on panels (d) and (f). The red stars (with white) show two characteristic peaks of the $P2_1/n$ phase on panel (e). Arrows on panel (d) show contributions from $SmMn_7O_{12}$ impurity in the x = 0.4 sample.

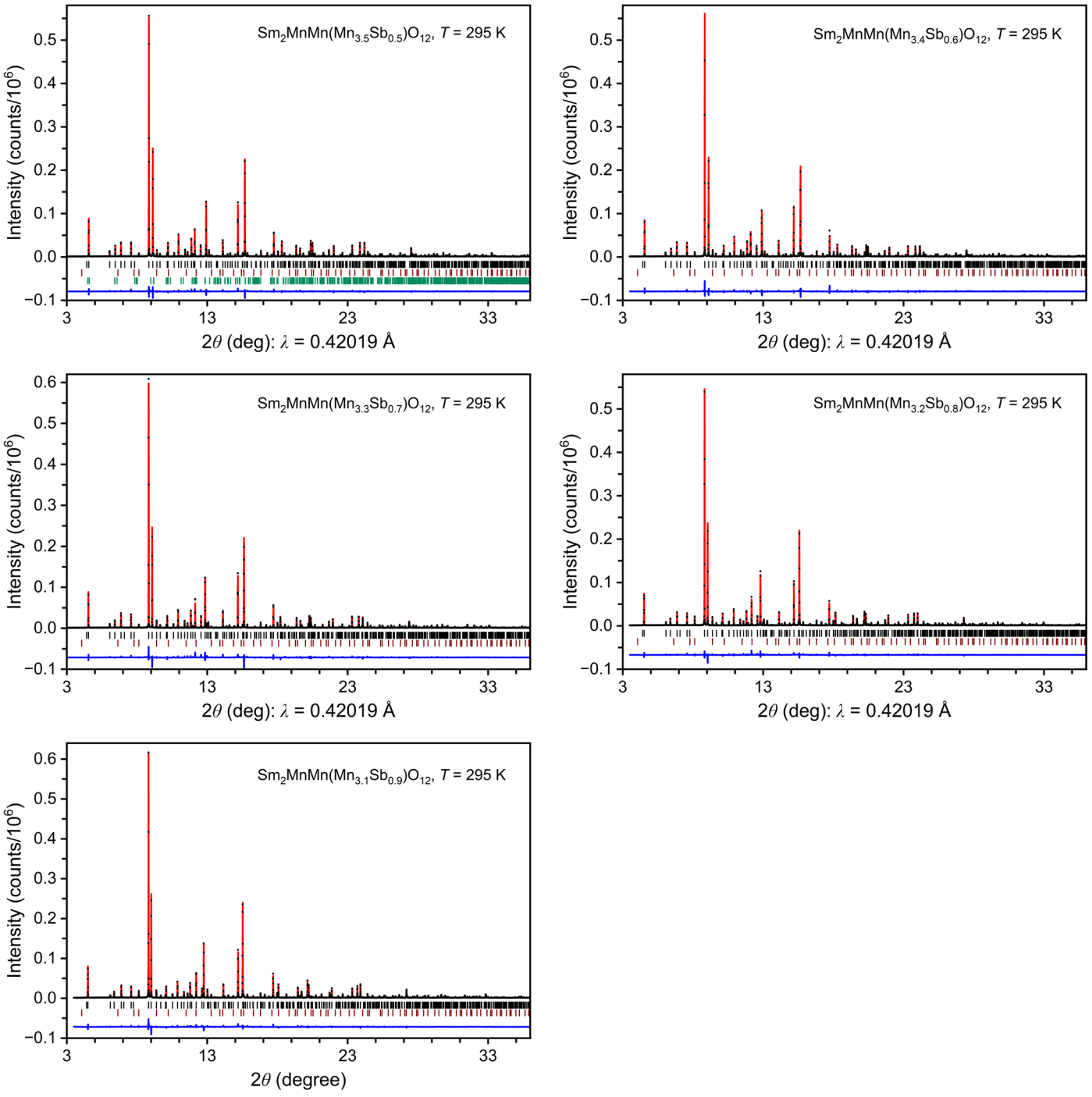

Figure S2. Fragments of experimental (black crosses), calculated (red line), and difference (blue line) synchrotron XRPD patterns of $Sm_2MnMn(Mn_{4-x}Sb_x)O_{12}$ with x = 0.5, 0.6, 0.7, 0.8, and 0.9 at T = 295 K. The tick marks show possible Bragg reflection positions of the main perovskite phase (the first row), pyrochlore impurity (the second row), and $SmMn_7O_{12}$ impurity (the third row, only appears in the sample with x = 0.5).

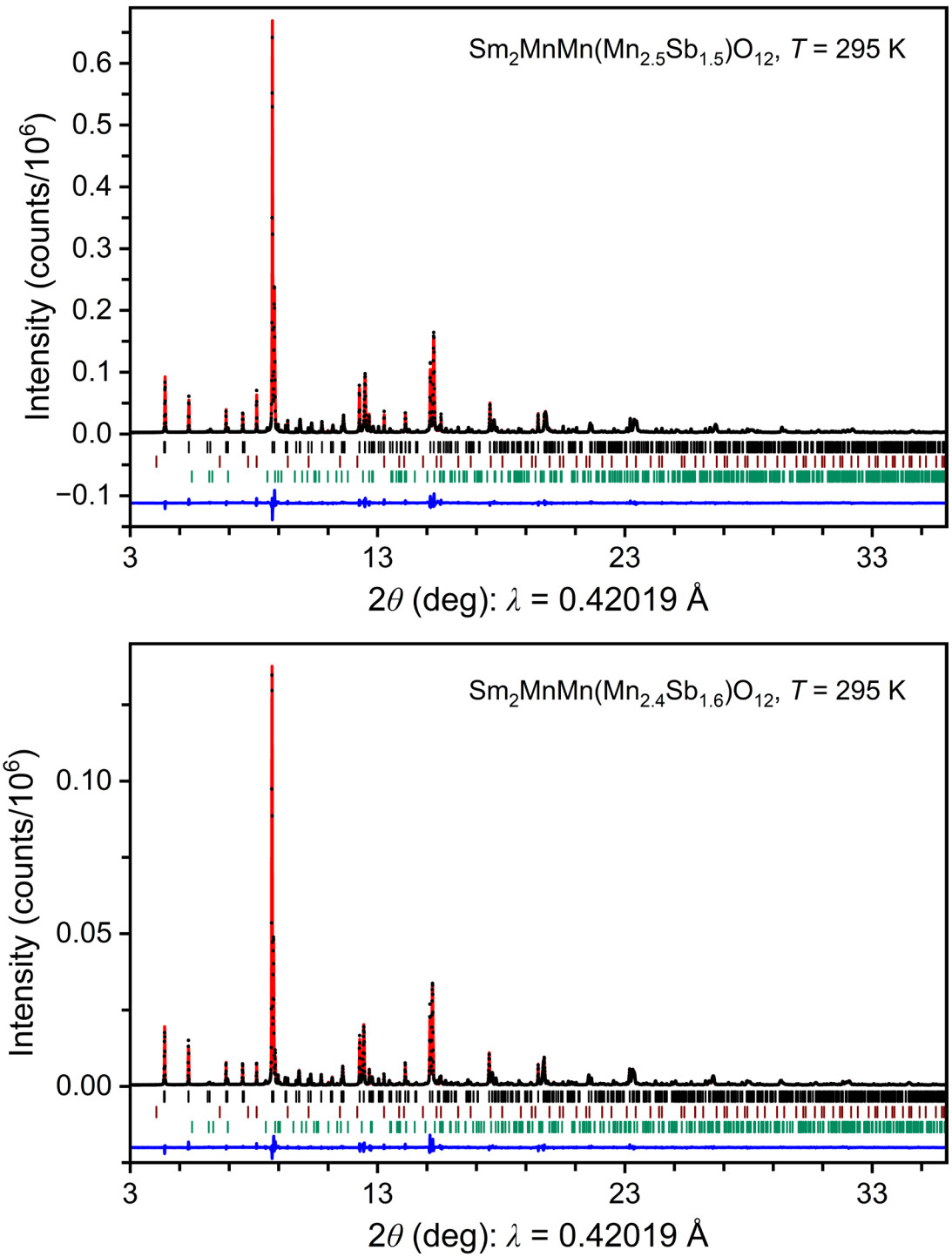

Figure S3. Fragments of experimental (black crosses), calculated (red line), and difference (blue line) synchrotron XRPD patterns of $Sm_2MnMn(Mn_{4-x}Sb_x)O_{12}$ with $x = 1.5$ and 1.6 at $T = 295$ K. The tick marks show possible Bragg reflection positions of the main perovskite phase (the first row), pyrochlore impurity (the second row), and impurity with *Pnma* symmetry (the third row).

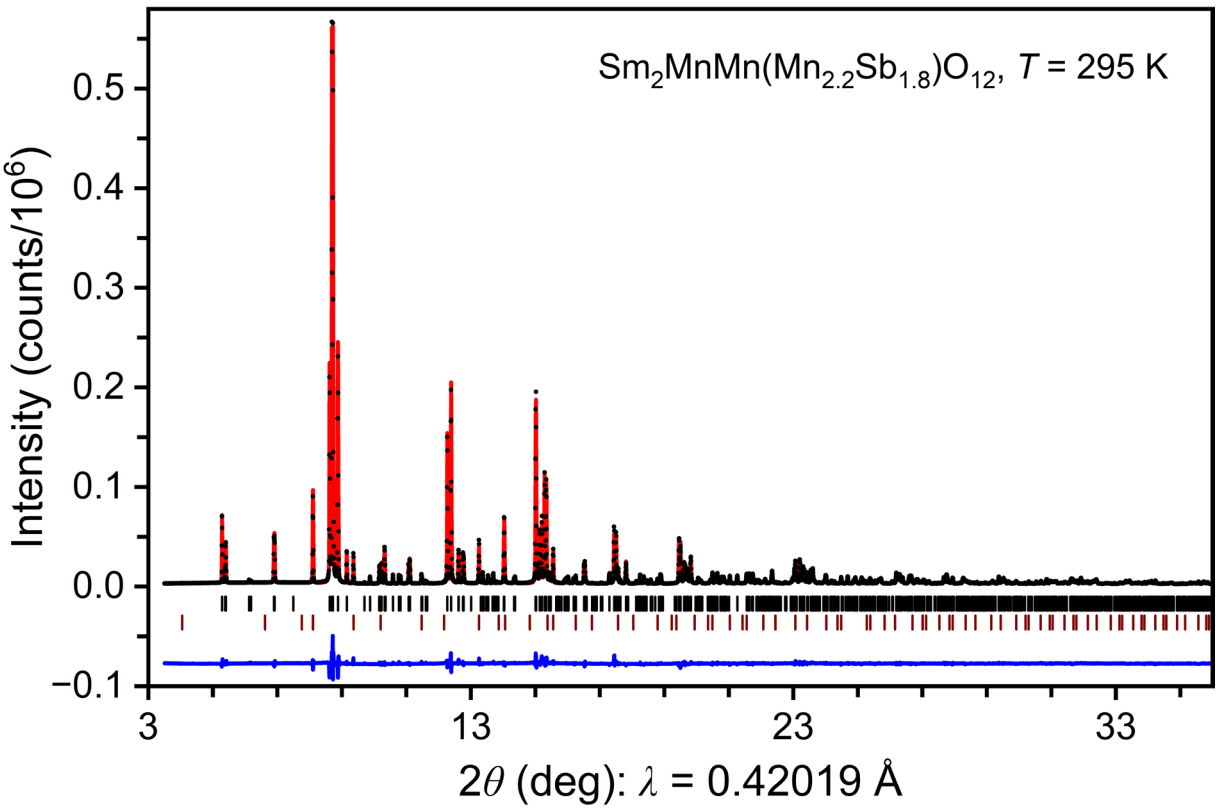

Figure S4. Fragments of experimental (black crosses), calculated (red line), and difference (blue line) synchrotron XRPD patterns of $Sm_2MnMn(Mn_{4-x}Sb_x)O_{12}$ with $x = 1.8$ at $T = 295$ K. The tick marks show possible Bragg reflection positions of the main perovskite phase (the first row) and pyrochlore impurity (the second row).

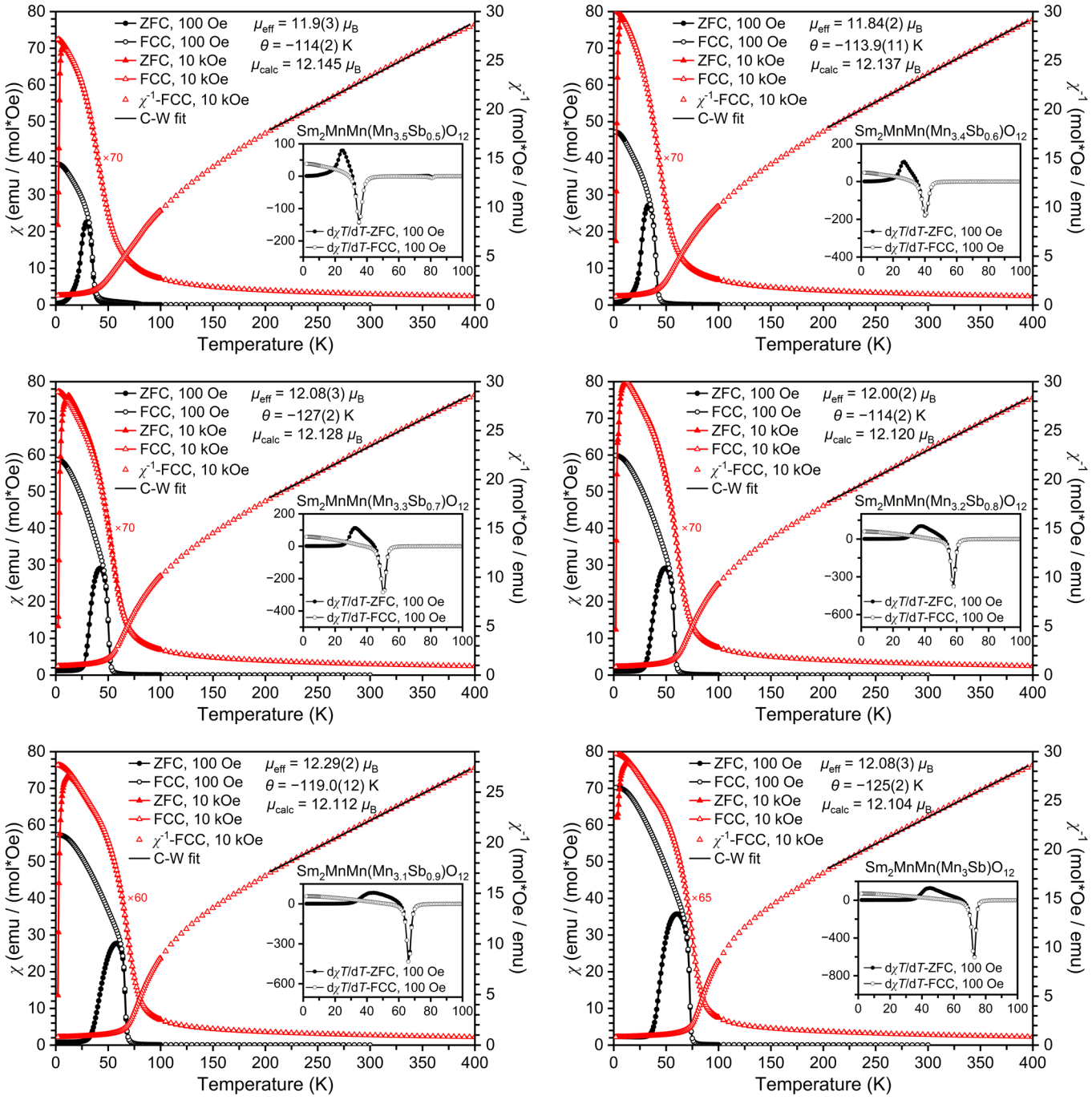

Figure S5. Left-hand axes: ZFC (filled symbols) and FCC (empty symbols) dc magnetic susceptibility ($\chi = M/H$) curves of $Sm_2MnMn(Mn_{4-x}Sb_x)O_{12}$ with $0.5 \le x \le 1.0$ measured at 100 Oe (black, circles) and 10 kOe (red, triangles). Right-hand axes: the FCC χ^{-1} versus T curve at 10 kOe; the black line gives the Curie–Weiss fit (C–W fit). The inset shows 100 Oe ZFC and FCC $d\chi T/dT$ versus T curves.

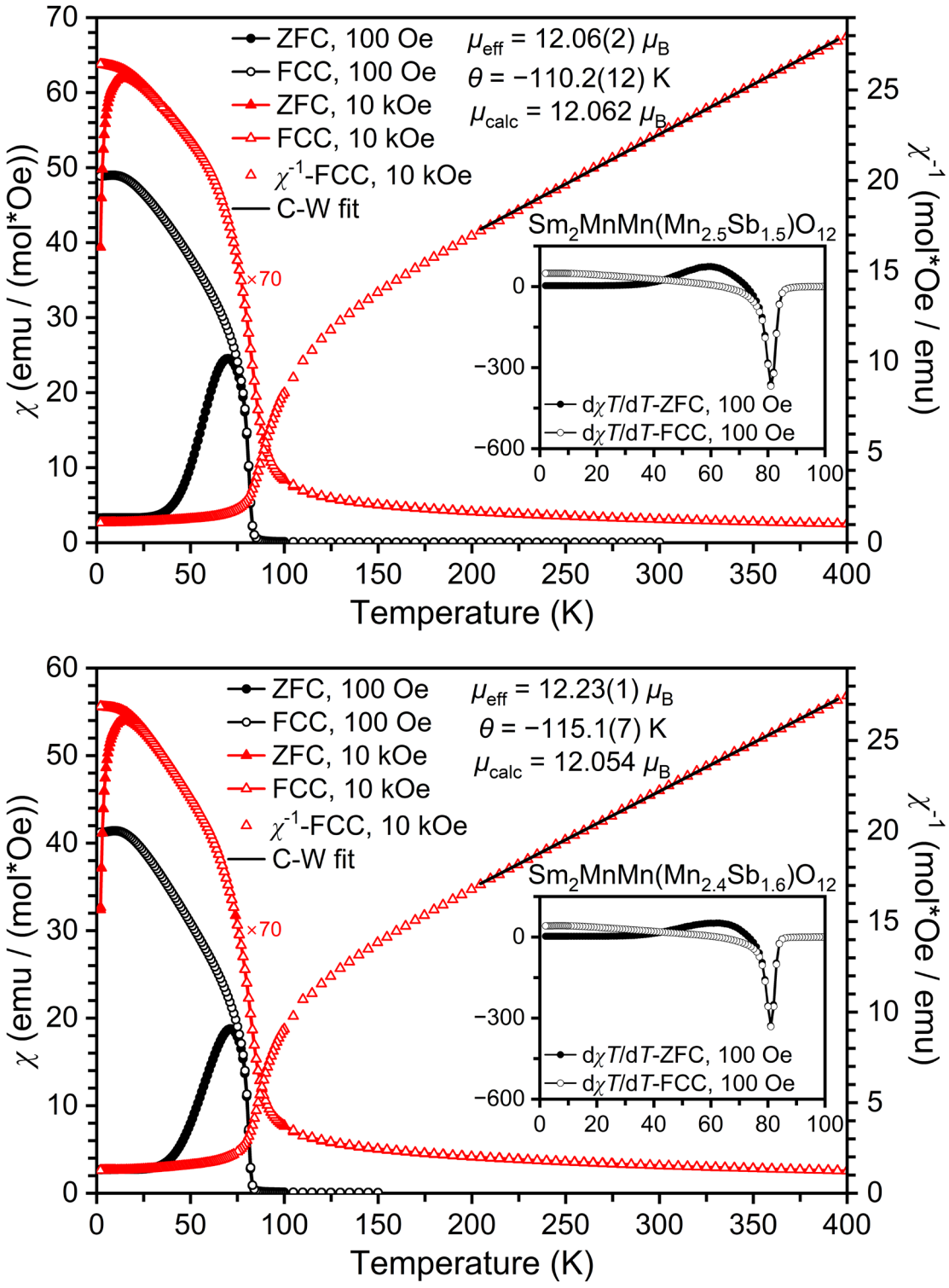

Figure S6. Left-hand axes: ZFC (filled symbols) and FCC (empty symbols) dc magnetic susceptibility ($\chi = M/H$) curves of $Sm_2MnMn(Mn_{4-x}Sb_x)O_{12}$ with $x = 1.5$ and 1.6 measured at 100 Oe (black, circles) and 10 kOe (red, triangles). Right-hand axes: the FCC χ^{-1} versus T curve at 10 kOe; the black line gives the Curie–Weiss fit (C–W fit). The inset shows 100 Oe ZFC and FCC $d\chi T/dT$ versus T curves.

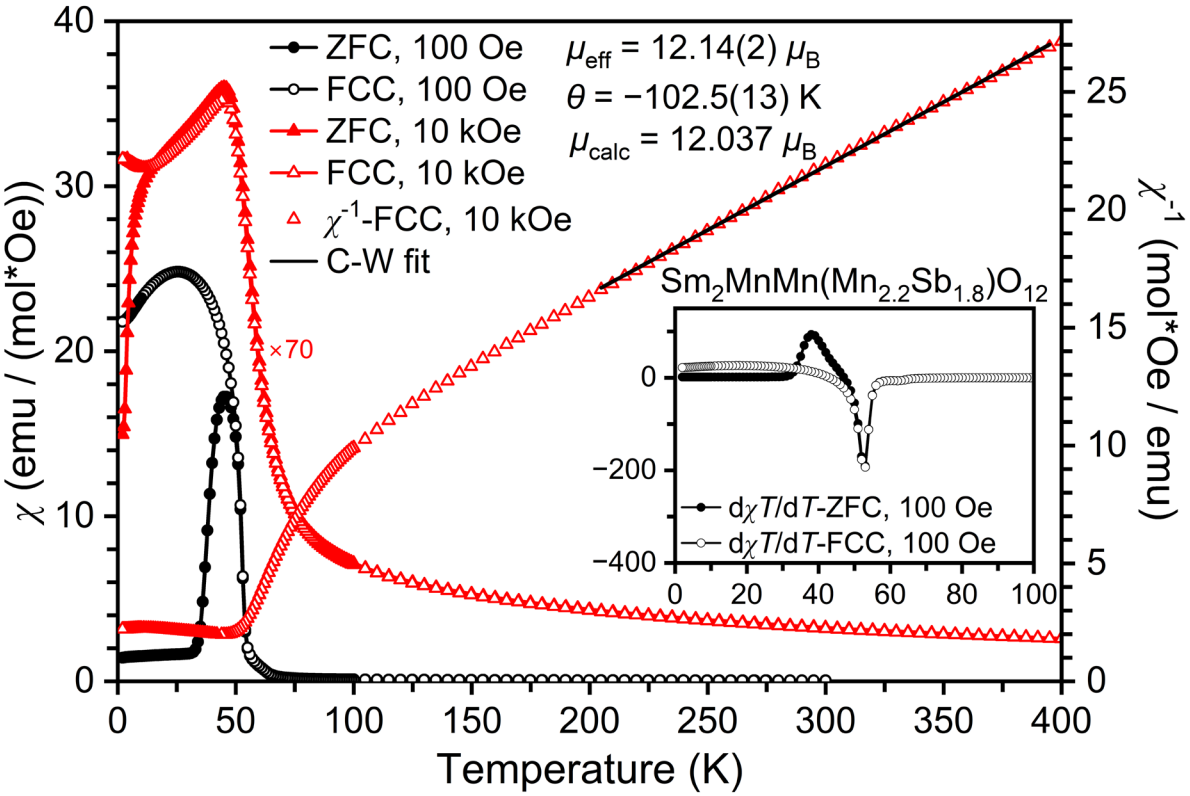

Figure S7. Left-hand axis: ZFC (filled symbols) and FCC (empty symbols) dc magnetic susceptibility ($\chi = M/H$) curves of $Sm_2MnMn(Mn_{4-x}Sb_x)O_{12}$ with $x = 1.8$ measured at 100 Oe (black, circles) and 10 kOe (red, triangles). Right-hand axis: the FCC χ^{-1} versus T curve at 10 kOe; the black line gives the Curie–Weiss fit (C–W fit). The inset shows 100 Oe ZFC and FCC $d\chi T/dT$ versus T curves.

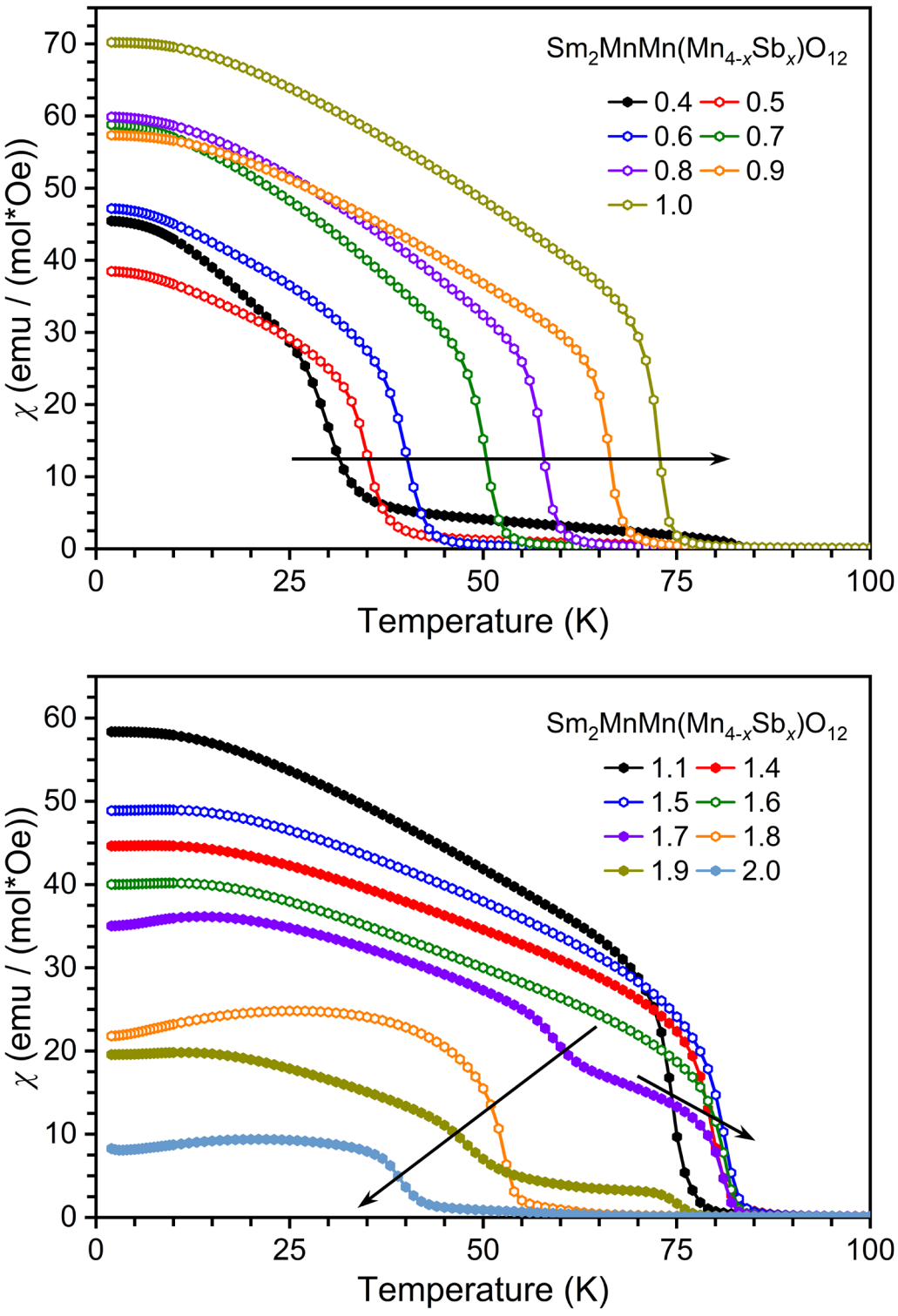

Figure S8. Comparison of FCC dc magnetic susceptibility ($\chi = M/H$) curves (filled symbols for samples with multi-phase and empty symbols for samples with single phase) of $Sm_2MnMn(Mn_{4-x}Sb_x)O_{12}$ with $0.4 \leq x \leq 1.0$ and $1.4 \leq x \leq 2.0$ measured at 100 Oe.

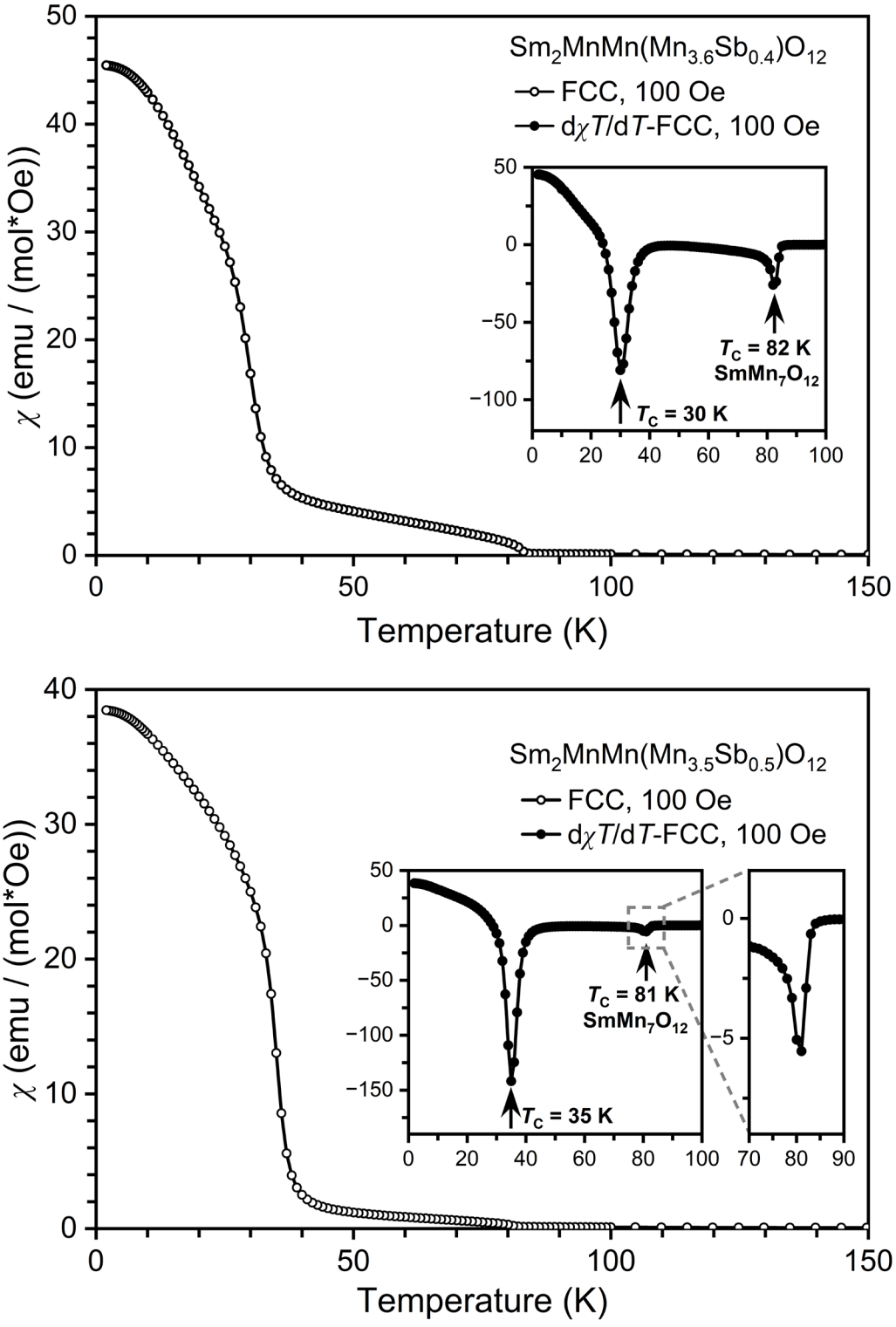

Figure S9. FCC dc magnetic susceptibility ($\chi = M/H$) curves of $Sm_2MnMn(Mn_{4-x}Sb_x)O_{12}$ with x = 0.4 and 0.5 measured at 100 Oe. The inset shows 100 Oe FCC $d\chi T/dT$ versus T curves.

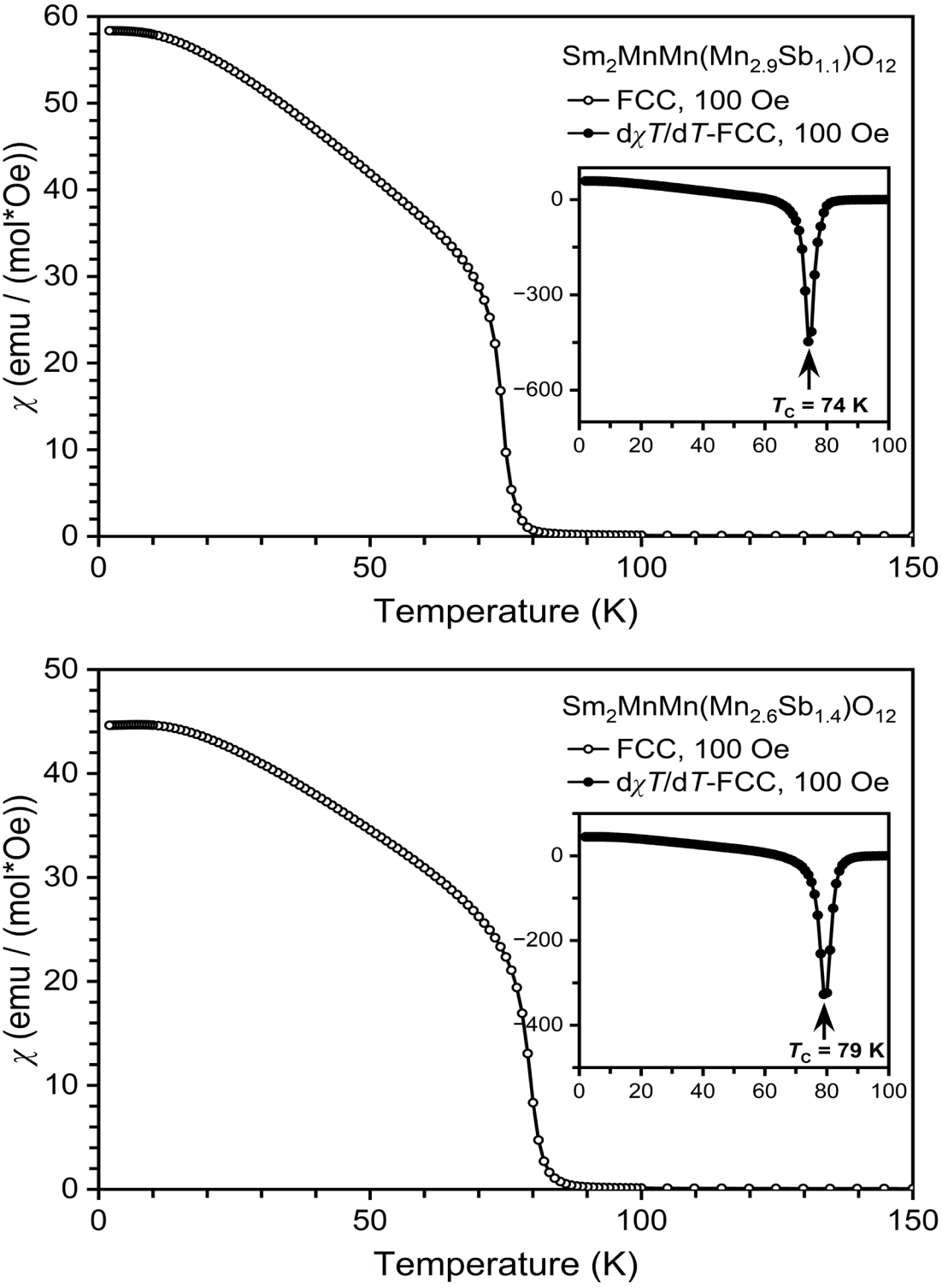

Figure S10. FCC dc magnetic susceptibility ($\chi = M/H$) curves of $Sm_2MnMn(Mn_{4-x}Sb_x)O_{12}$ with x = 1.1 and 1.4 measured at 100 Oe. The inset shows 100 Oe FCC $d\chi T/dT$ versus T curves.

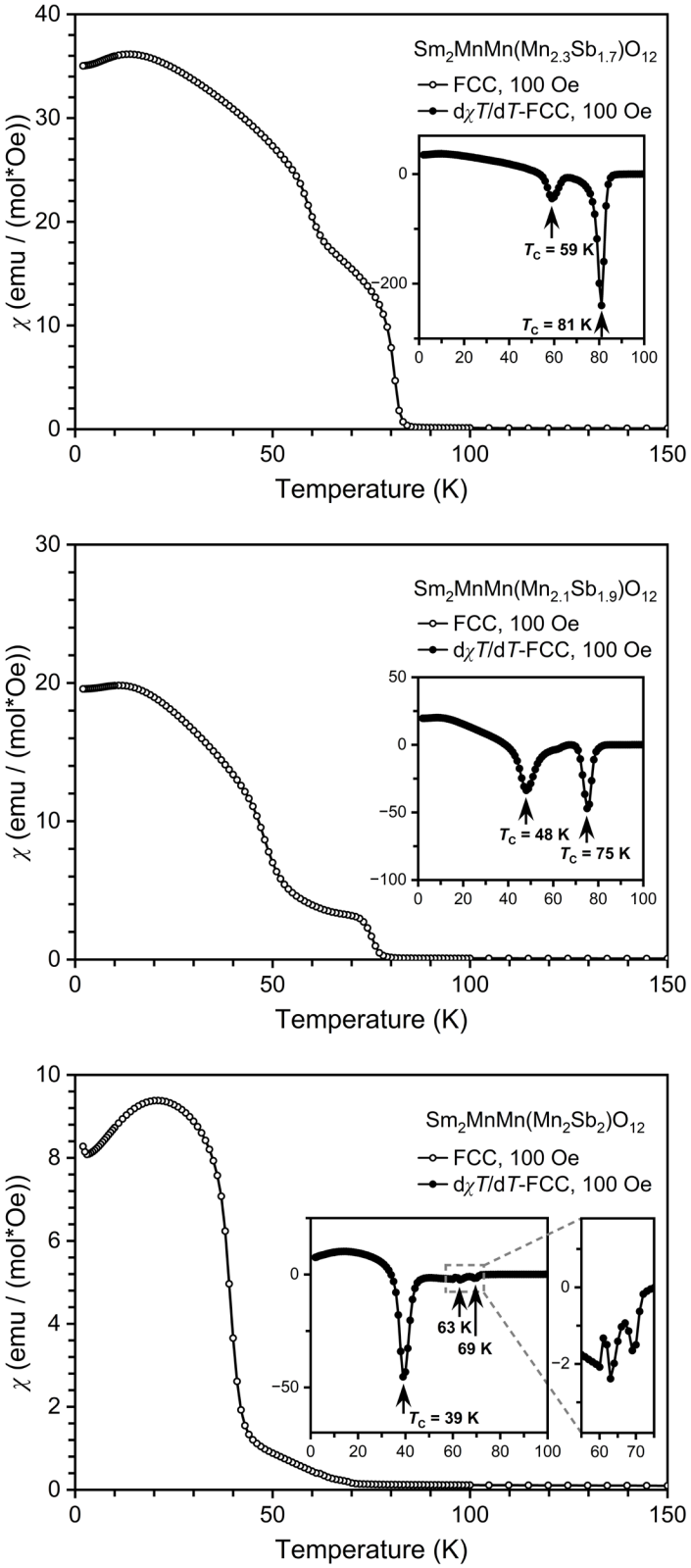

Figure S11. FCC dc magnetic susceptibility ($\chi = M/H$) curves of $Sm_2MnMn(Mn_{4-x}Sb_x)O_{12}$ with x = 1.7, 1.9, and 2.0 measured at 100 Oe. The inset shows 100 Oe FCC $d\chi T/dT$ versus T curves. Additional magnetic anomalies in the x = 2 sample could originate from an unidentified impurity.

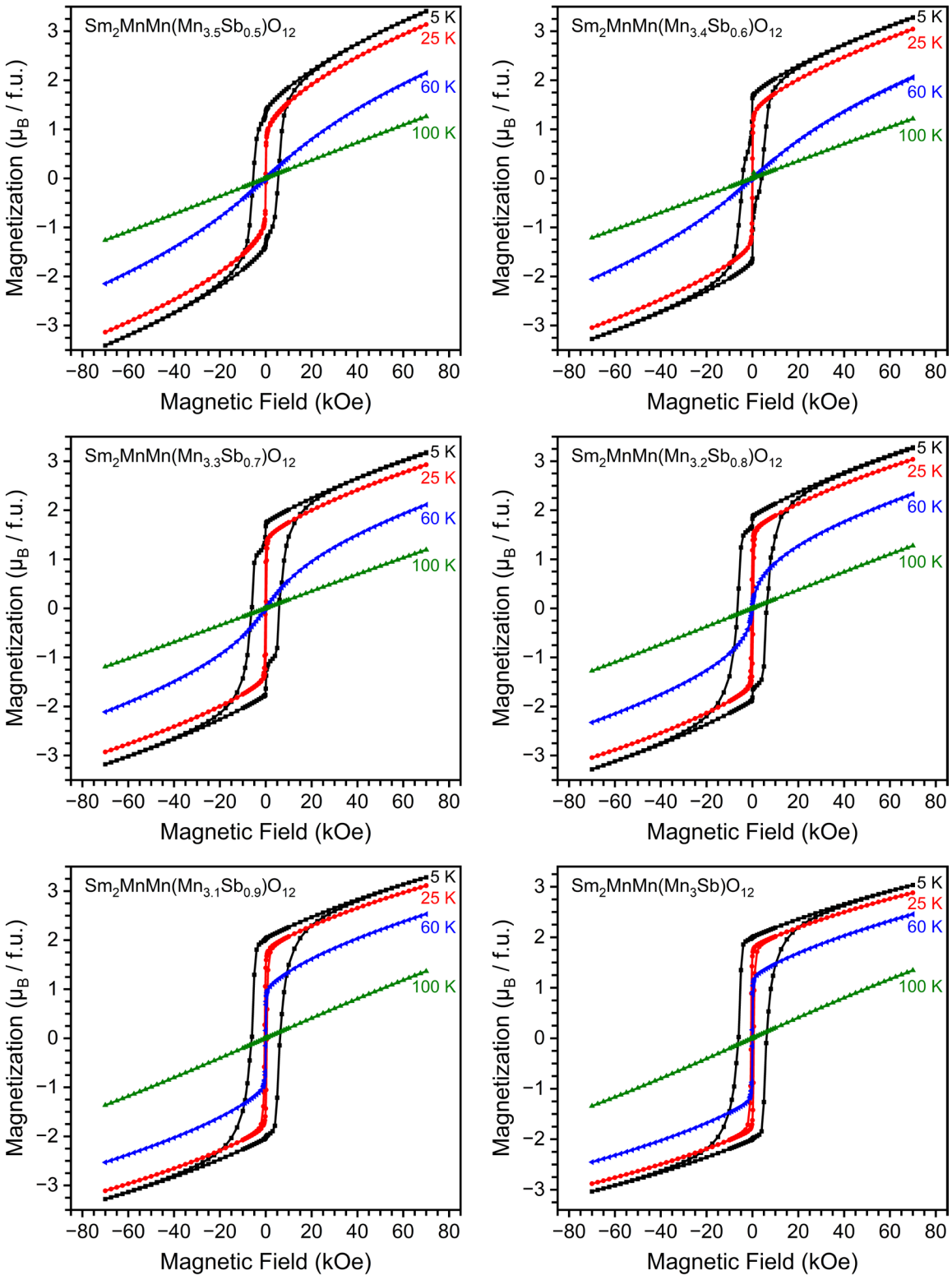

Figure S12. *M* versus *H* curves of $Sm_2MnMn(Mn_{4-x}Sb_x)O_{12}$ with $0.5 \leq x \leq 1.0$ at different temperatures.

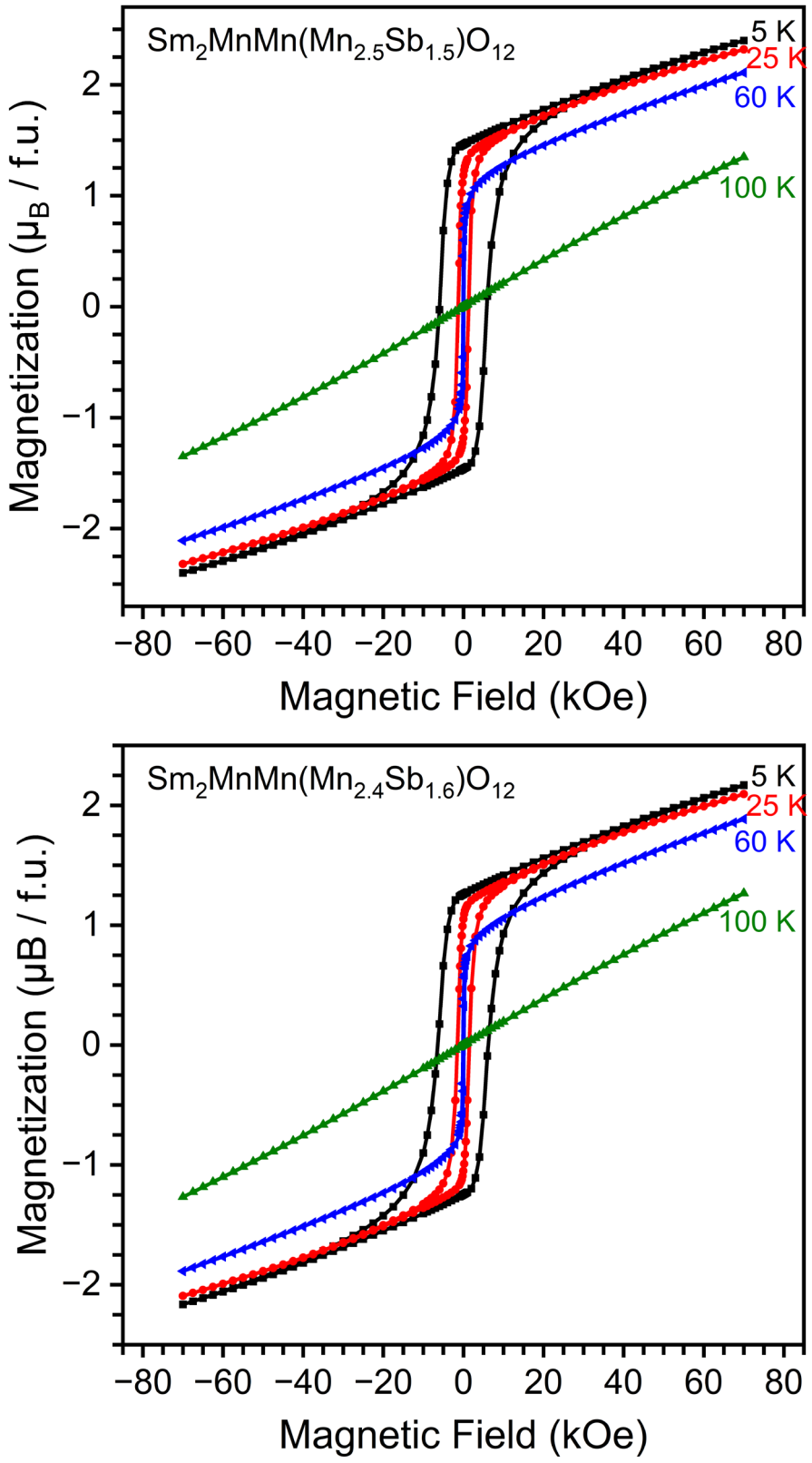

Figure S13. *M* versus *H* curves of $Sm_2MnMn(Mn_{4-x}Sb_x)O_{12}$ with x = 1.5 and 1.6 at different temperatures.

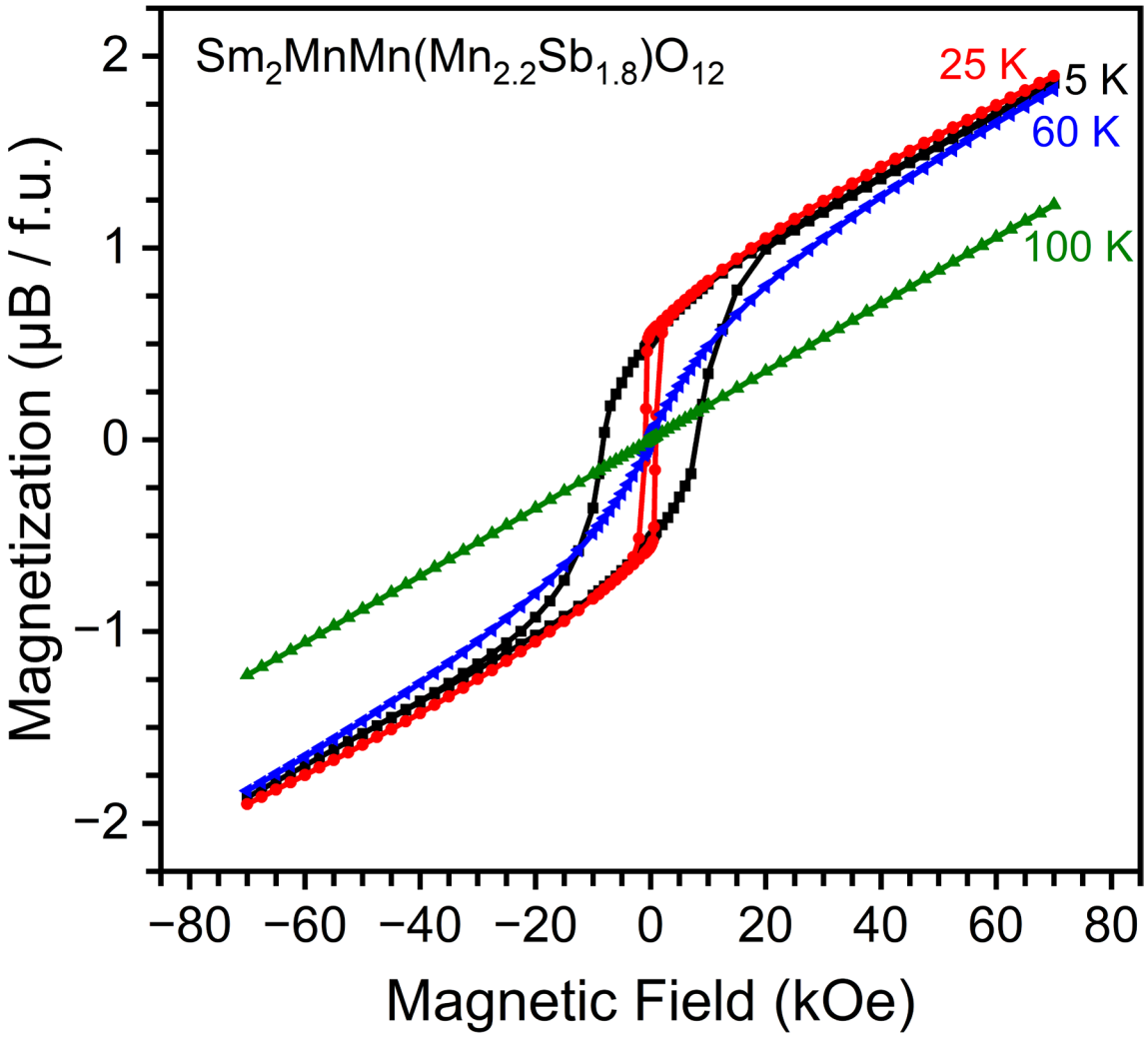

Figure S14. *M* versus *H* curves of $Sm_2MnMn(Mn_{4-x}Sb_x)O_{12}$ with x = 1.8 at different temperatures.

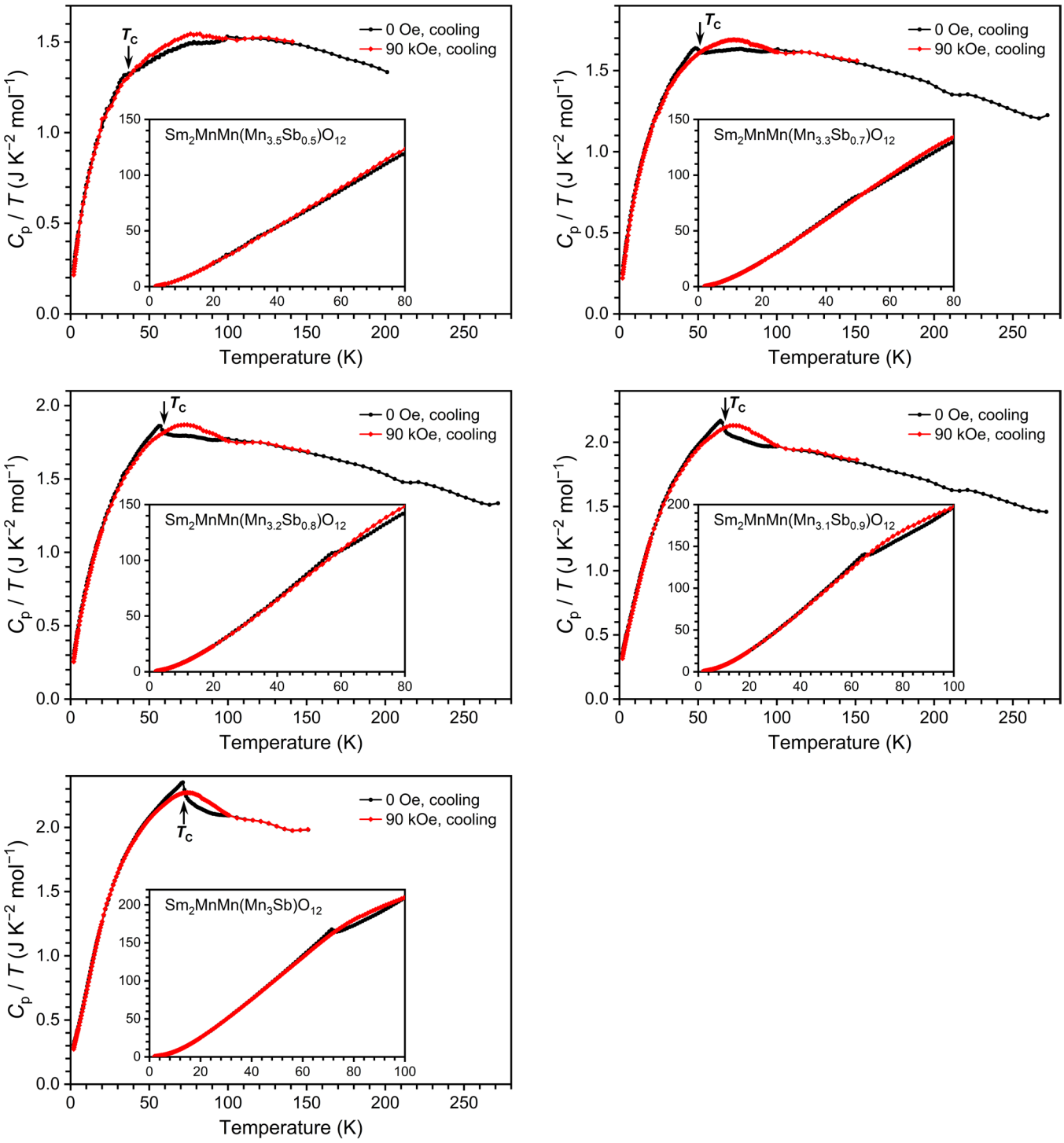

Figure S15. Specific heat data of $Sm_2MnMn(Mn_{4-x}Sb_x)O_{12}$ with x = 0.5, 0.7, 0.8, 0.9, and 1.0, plotted as C_p/T versus T. Measurements were performed on cooling at H = 0 Oe and 90 kOe. Insets present the C_p (in J K^{-1} mol^{-1}) versus T curves.

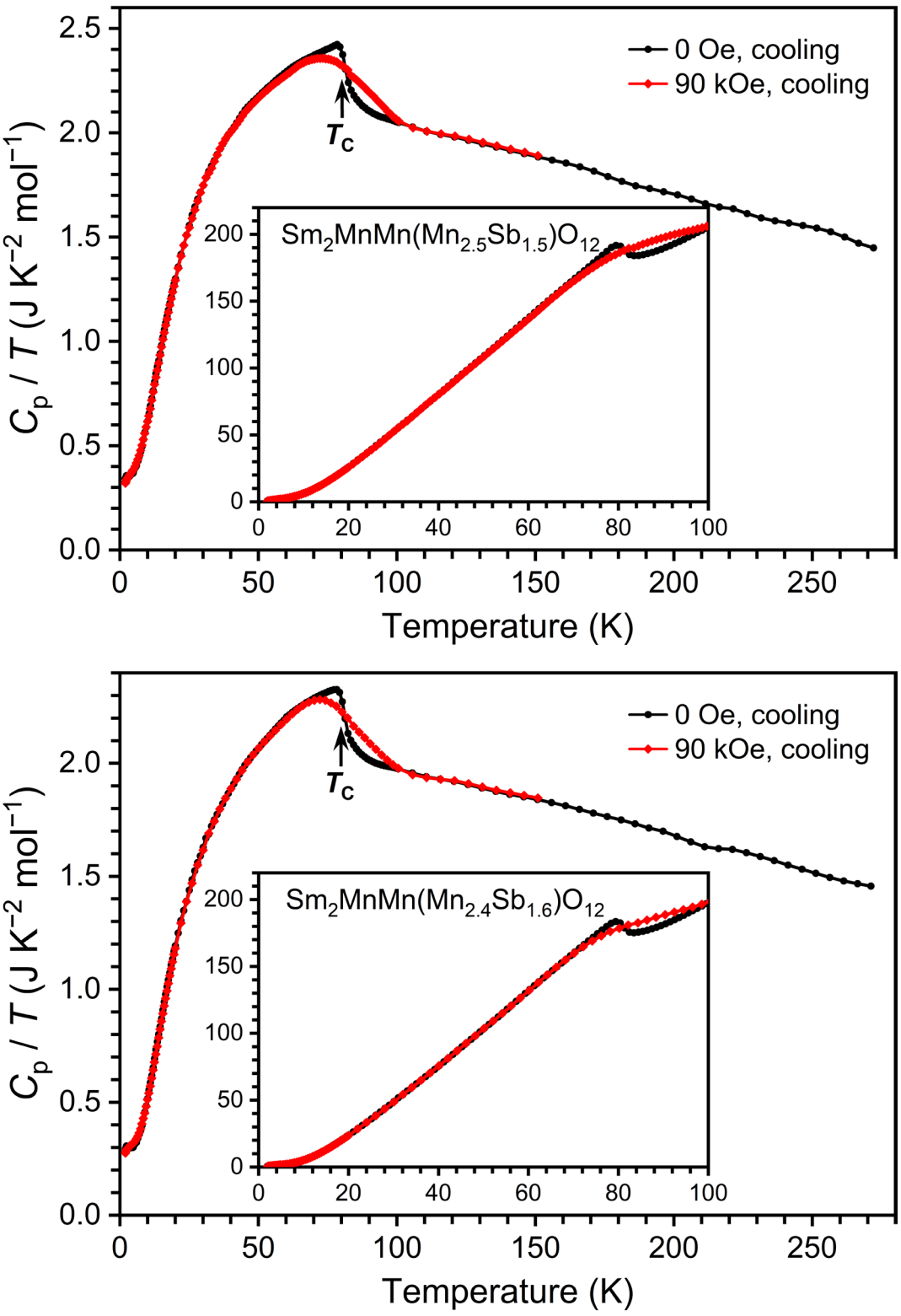

Figure S16. Specific heat data of $Sm_2MnMn(Mn_{4-x}Sb_x)O_{12}$ with x = 1.5 and 1.6, plotted as C_p/T versus T. Measurements were performed on cooling at H = 0 Oe and 90 kOe. Insets present the C_p (in J K^{-1} mol^{-1}) versus T curves.

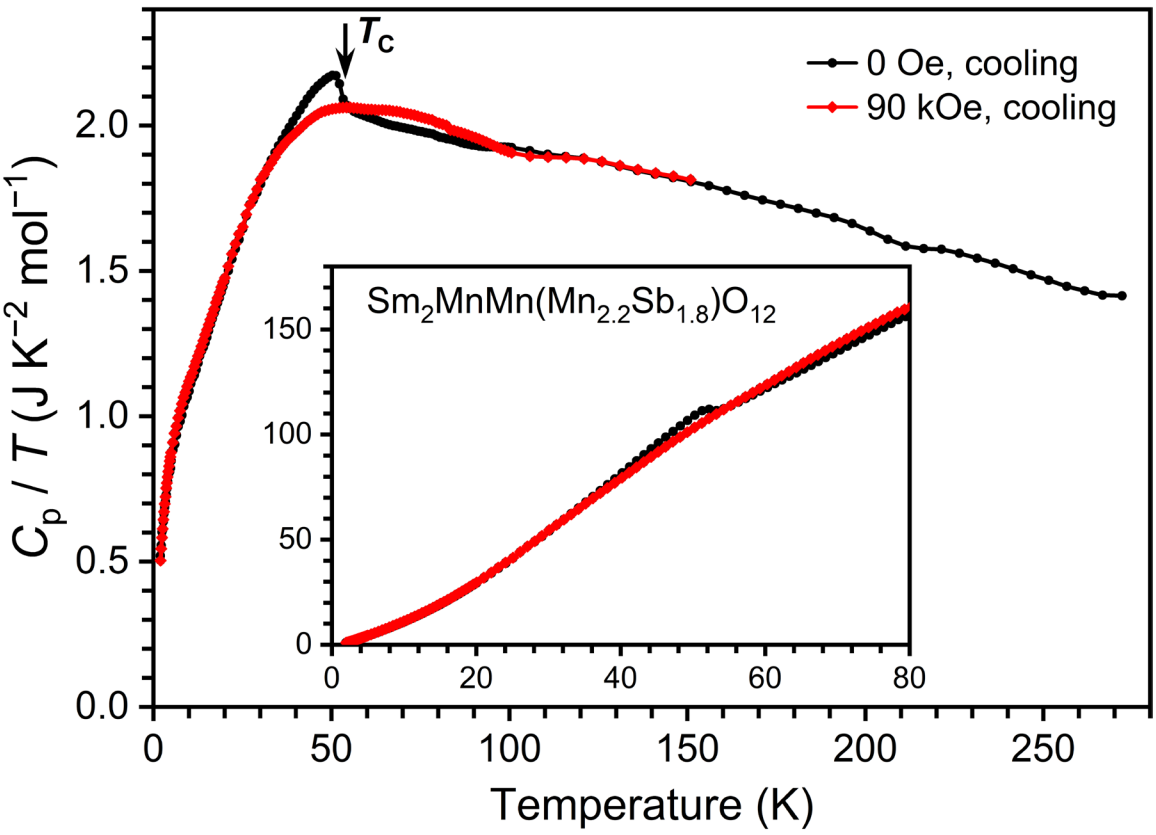

Figure S17. Specific heat data of $Sm_2MnMn(Mn_{4-x}Sb_x)O_{12}$ with x = 1.8, plotted as C_p/T versus T. Measurements were performed on cooling at H = 0 Oe and 90 kOe. Insets present the C_p (in J K^{-1} mol^{-1}) versus T curves.

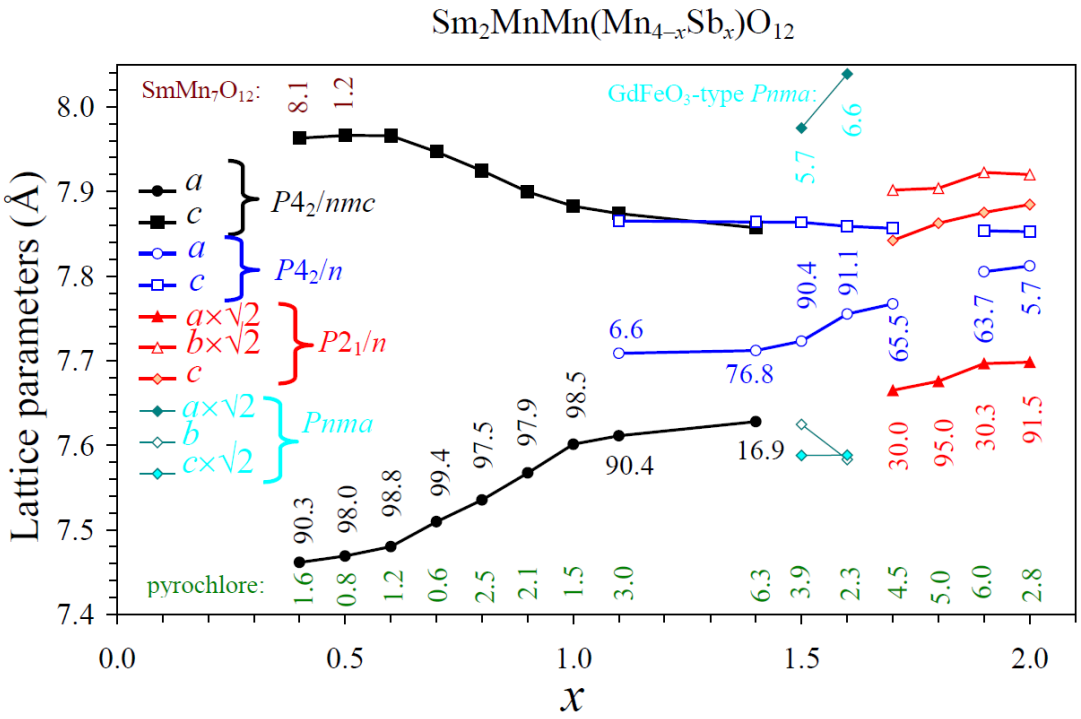

Figure S18. Compositional dependence of the lattice parameters (similar to Figure 2 in the main text) and weight fractions of all phases in the $Sm_2MnMn(Mn_{4-x}Sb_x)O_{12}$ solid solutions for $0.4 \le x \le 2.0$ from synchrotron XRPD data at room temperature. Numbers show weight fractions (in %) for all phases [$SmMn_7O_{12}$: brown; pyrochlore: green]. Note that only a ratio of the weight fractions of the phases is relevant (not absolute values) for the $x = 2$ sample because of the presence of an unidentified impurity in the $Sm_2MnMn(Mn_2Sb_2)O_{12}$ sample; all peaks of this unidentified impurity could be indexed in space group $R\bar{3}$ with $a = 7.4299$ Å and $c = 8.7800$ Å.

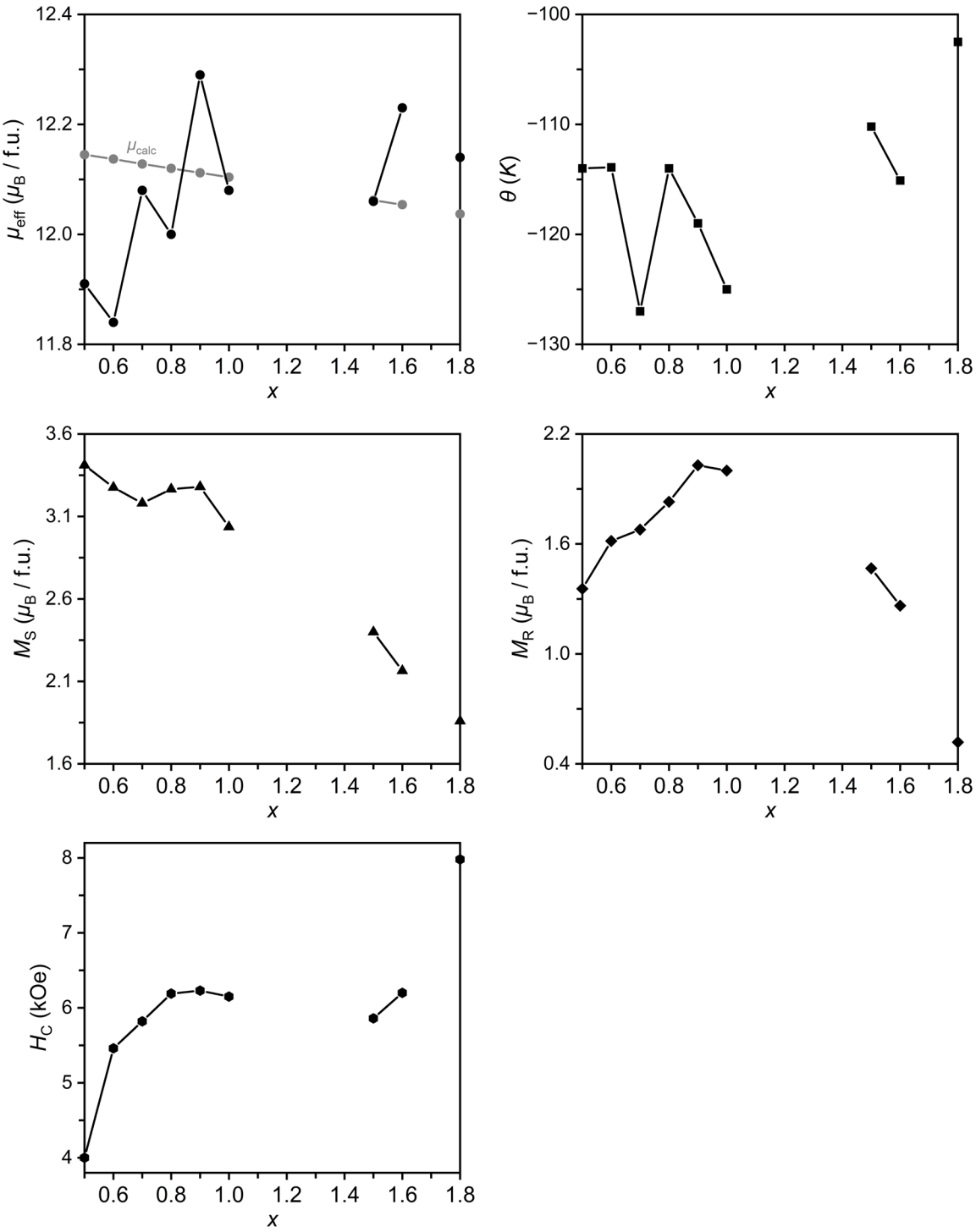

Figure S19. Compositional dependence of (left, up) the effective calculated and experimental magnetic moments, (right, up) Curie-Weiss temperatures and (middle, bottom) parameters of the *M* versus *H* curves in the $Sm_2MnMn(Mn_{4-x}Sb_x)O_{12}$ solid solutions (visualization of data reported in Table 1 in the main text).

Table S10. Results of refinements of occupation factors of the cation sites in $Sm_2MnMn(Mn_{4-x}Sb_x)O_{12}$ (x = 0.5, 0.6, and 0.7); space group $P4_2/nmc$; SQ: square-planar, T: tetrahedral, Oc: octahedral. These results were used in Figure 3c of the main text.

	x		
	0.5	0.6	0.7
g(Sm) [a]	0.9571(17)	0.9480(18)	0.9594(21)
B(Sm) (Å^2)	1.079(8)	1.122(10)	1.200(11)
g(Mn1-SQ)	0.568(3)	0.578(4)	0.565(5)
B(Mn1) (Å^2)	1.53(8)	1.41(8)	1.95(11)
g(Mn2-T)	1.129(6)	1.100(6)	1.136(8)
B(Mn2) (Å^2)	0.56(4)	0.52(4)	0.64(6)
g(Mn/Sb-Oc) [a] fixed	0.875Mn+0.125Sb	0.85Mn+0.15Sb	0.825Mn+0.175Sb
B(Mn/Sb) (Å^2)	0.710(12)	0.762(14)	0.847(17)
g(Mn/Sb-Oc) [b]	0.877(2)Mn+0.123Sb	0.851(2)Mn+0.149Sb	0.833(3)Mn+0.167Sb
B(Mn/Sb) (Å^2)	0.700(13)	0.756(15)	0.815(17)

[a] All structural and non-structural parameters were refined simultaneously except the occupation factors, g(Mn/Sb-Oc), of the Mn/Sb-Oc site, which were fixed at the nominal values. In this model, only Sm was assumed at the Sm site, and only Mn – at the Mn1-SQ and Mn2-T sites. Deviations from 1 (or from 0.5 for the split Mn1-SQ site) indicate the presence of small anti-site disorders.

[b] All structural and non-structural parameters were refined simultaneously except the g(Sm) site (g(Sm) was fixed at the value reported in Table S2), and the refinements in this model started from the results reported in Table S2. The following constraint was used, g(Sb) = 1 – g(Mn), for the Mn/Sb-Oc site. These results demonstrate that the refined occupations of the Mn/Sb-Oc site were close to the nominal values; therefore, they were fixed to the nominal values in the final models reported in Table S2.

Table S11. Results of refinements of occupation factors of the cation sites in $Sm_2MnMn(Mn_{4-x}Sb_x)O_{12}$ (x = 0.8, 0.9, and 1.0); space group $P4_2/nmc$; SQ: square-planar, T: tetrahedral, Oc: octahedral. These results were used in Figure 3c of the main text.

	x		
	0.8	0.9	1.0
g(Sm) [a]	0.9527(17)	0.9424(17)	0.9470(17)
B(Sm) (Å^2)	1.194(10)	1.317(10)	1.315(11)
g(Mn1-SQ)	0.578(4)	0.587(4)	0.599(4)
B(Mn1) (Å^2)	1.53(9)	1.86(9)	1.71(8)
g(Mn2-T)	1.147(7)	1.134(7)	1.092(6)
B(Mn2) (Å^2)	0.76(5)	0.75(5)	0.59(5)
g(Mn/Sb-Oc) [a] fixed	0.8Mn+0.2Sb	0.775Mn+0.225Sb	0.75Mn+0.25Sb
B(Mn/Sb) (Å^2)	0.782(13)	0.902(15)	0.830(13)
g(Mn/Sb-Oc) [b]	0.805(2)Mn+0.195Sb	0.779(2)Mn+0.221Sb	0.753(2)Mn+0.247Sb
B(Mn/Sb) (Å^2)	0.761(14)	0.880(15)	0.817(14)

[a] All structural and non-structural parameters were refined simultaneously except the occupation factors, g(Mn/Sb-Oc), of the Mn/Sb-Oc site, which were fixed at the nominal values. In this model, only Sm was assumed at the Sm site, and only Mn – at the Mn1-SQ and Mn2-T sites. Deviations from 1 (or from 0.5 for the split Mn1-SQ site) indicate the presence of small anti-site disorders.

[b] All structural and non-structural parameters were refined simultaneously except the g(Sm) site (g(Sm) was fixed at the value reported in Table S4), and the refinements in this model started from the results reported in Table S4. The following constraint was used, g(Sb) = 1 – g(Mn), for the Mn/Sb-Oc site. These results demonstrate that the refined occupations of the Mn/Sb-Oc site were close to the nominal values; therefore, they were fixed to the nominal values in the final models reported in Table S4.

Table S12. Results of refinements of occupation factors of the cation sites in $Sm_2MnMn(Mn_{4-x}Sb_x)O_{12}$ (x = 1.5 and 1.6); space group $P4_2/n$; SQ: square-planar, T: tetrahedral, Oc: octahedral. These results were used in Figure 3c of the main text.

	x	
	1.5	1.6
g(Sm) [a]	0.946(4)	0.955(4)
B(Sm) (Å^2)	1.079(17)	0.949(16)
g(Mn1-SQ)	0.618(5)	0.621(6)
B(Mn1) (Å^2)	1.84(11)	1.87(12)
g(Mn2-T)	1.036(9)	1.002(9)
B(Mn2) (Å^2)	0.26(7)	0.10(6)
g(Mn3-Oc) [a]	1 fixed	1 fixed
B(Mn3) (Å^2)	0.82(5)	0.78(4)
g(Sb-Oc)	0.877(4)	0.915(4)
B(Sb) (Å^2)	0.63(2)	0.49(2)
g(Mn3-Oc) [b]	1.000(4)	0.991(4)
B(Mn3) (Å^2)	0.82(5)	0.80(5)
g(Sb-Oc)	0.749(5)Sb+0.251Mn	0.806(5)Sb+0.194Mn
B(Sb) (Å^2)	0.58(2)	0.46(2)

[a] All structural and non-structural parameters were refined simultaneously except for the occupation factors, g(Mn3-Oc), of the Mn3-Oc site, which were fixed at unity. In this model, only Sm was assumed at the Sm site, only Mn – at the Mn1-SQ, Mn2-T, and Mn3-Oc sites, and only Sb – at the Sb-Oc site. Deviations from 1 (or from 0.5 for the split Mn1-SQ site) indicate the presence of small anti-site disorders.

[b] All structural and non-structural parameters were refined simultaneously except for the g(Sm) site (g(Sm) was fixed at the value reported in Table S6), and the refinements in this model started from the results reported in Table S6. The following constraint was used, g(Mn) = 1 – g(Sb), for the Sb-Oc site. These results demonstrate that the refined occupations of the Sb-Oc site were close to the nominal values, and the refined occupations of the Mn3-Oc site were close to 1; therefore, they were fixed to the nominal values in the final models reported in Table S6.

Table S13. Results of refinements of occupation factors of the cation sites in $Sm_2MnMn(Mn_{4-x}Sb_x)O_{12}$ (x = 1.8); space group $P2_1/n$; Oc: octahedral. These results were used in Figure 3c of the main text.

	x
	1.8
g(Sm/Mn) [a]	0.5Sm+0.5Mn fixed
B(Sm) (Å^2)	0.915(11)
g(Mn-Oc)	0.996(3)
B(Mn) (Å^2)	0.79(3)
g(Sb-Oc)	0.937(2)
B(Sb) (Å^2)	0.571(15)
g(Sm/Mn) [b]	0.499(4)Sm+0.501Mn
B(Sm) (Å^2)	0.910(11)
g(Mn-Oc)	1 fixed
B(Mn) (Å^2)	0.81(3)
g(Sb/Mn-Oc)	0.871(7)Sb+0.129Mn
B(Sb/Mn) (Å^2)	0.551(15)

[a] All structural and non-structural parameters were refined simultaneously except for the occupation factor, g(Sm/Mn) = 0.5Sm+0.5Mn, of the Sm/Mn site. In this model, only Mn was assumed at the Mn-Oc sites, and only Sb – at the Sb-Oc site.

[b] All structural and non-structural parameters were refined simultaneously except g(Mn-Oc) = 1 The following constraints were used, g(Mn) = 1 – g(Sm), for the Sm/Mn site and g(Mn) = 1 – g(Sb), for the Sb/Mn site. These results show that g(Sm/Mn) and g(Sb/Mn-Oc) were close to the target, nominal values; therefore, they were fixed to the nominal values in the final model reported in Table S8.

References

[29] S. Kawaguchi, M. Takemoto, K. Osaka, E. Nishibori, C. Moriyoshi, Y. Kubota, Y. Kuroiwa, K. Sugimoto, *Rev. Sci. Instrum.* **2017**, *88*, 085111.

[30] F. Izumi, T. Ikeda, *Mater. Sci. Forum* **2000**, *321–324*, 198–205.

[31] N. E. Brese, M. O'Keeffe, *Acta Crystallogr., Sect. B: Struct. Sci.* **1991**, *47*, 192–197.